Engineering Geology 301 (2022) 106594

Contents lists available at ScienceDirect

Engineering Geology

journal homepage: www.elsevier.com/locate/enggeo

Seismic response of stratified rock slopes due to incident P and SV waves using a semi-analytical approach

Mengtao Wu [a,b], Fangcheng Liu [b,*], Jun Yang [c,*]

[a] Department of Civil Engineering, Tianjin University, Tianjin 300350, China
[b] College of Civil Engineering, Hunan University of Technology, Zhuzhou 412007, China
[c] Department of Civil Engineering, The University of Hong Kong, Pokfulam, Hong Kong

ARTICLE INFO

Keywords:
Stratified rock slope
Wave propagation and scattering
Peak ground acceleration
Spectral response
Seismic wave field
Semi-analytical approach

ABSTRACT

Based on the theory of elastodynamics and the concept of wave-field separation, a semi-analytical method for the scattering and diffraction of P-SV waves by stratified rock slopes is proposed in this study. The total wave fields are decomposed into the free field with no irregularity and the scattered wave field generated by slope topography. The former is solved directly with the aid of a dynamic stiffness matrix, and the latter is modeled by applying the inclined and horizontal fictitious distributed loads on the corresponding boundaries. Since the methodology is derived from the exact wave equations and the non-singular frequency-domain Green's functions, it can be applied to seismic dynamic response problems for layered slopes with arbitrary incident waves and layer thicknesses, and the presented solutions are high-precision and well-converged. Using a Ricker wavelet as input, the accuracy and effectiveness of the proposed method for both vertically and obliquely incident P and SV waves are fully verified. Taking three actual earthquake records including Taft wave, El Centro wave, and Loma Prieta wave as inputs, several analysis examples are presented. The parametric studies demonstrate that a significant elevation amplification effect can be seen in the ground motion of rock slopes due to the interaction of the upper slope feature with the underlying bedrock half-space. The PGA amplification factor, Fourier spectrum and standard spectral ratio of rock slopes are evidently affected by the slope height, slope angle and shear velocity of the medium. Subsequently, sensitivity analyses are performed on model slopes with varying incident wave frequencies and incident angles to illustrate the broad applicability of the proposed method. Finally, a case study is presented to evaluate the practicality of the presented procedure and highlight the benefits of performing a rapid semi-analytical solution to assess potential hazards of earthquake-induced rock slides.

1. Introduction

In recent years, due to the frequent occurrence of seismic events, slope instability induced by earthquake ground motion has become the most common secondary hazard in many countries and regions. As in the 2008 Wenchuan earthquake, the mainshock and aftershock sequences triggered more than 15,000 landslides, causing about one-third of a total number of casualties and hundreds of billions of direct economic losses (Yin et al., 2009; Tang et al., 2011). On the other hand, numerous large-scale infrastructures are constructed in tectonically active zones with high and steep rock slopes. For example, the left bank slope of the Jinping first-stage hydropower station located on the Yalong River, Southwest China, is a huge complex rock block with multiple structural surfaces, where earthquake-triggered rock slope failures may be a major hidden danger threatening the safety of this project (Huang et al., 2010; Li et al., 2015). Therefore, the assessment of the dynamic stability of rock slopes under earthquake loading is of great theoretical and engineering significance for guiding earthquake-induced landslide prediction and earthquake-resistant fortification.

In general, dynamic slope stability analysis is a challenging subject at the intersection of multidisciplinary fields such as geological engineering, geotechnical engineering, and seismology. The scattering and diffraction of compressional (P-) and shear (S-) waves by slope topography is an essential factor affecting the deformation and failure of earthquake-induced landslides, and is also the theoretical foundation of slope stability analysis. It is generally believed that the seismic responses of rock slopes are closely related to the slope features, geological conditions, and seismic sources. Currently, the research methods mainly

* Corresponding authors at: College of Civil Engineering, Hunan University of Technology, Zhuzhou 412007, China.
E-mail addresses: wumengtao@tju.edu.cn (M. Wu), fcliu@hut.edu.cn (F. Liu), junyang@hku.hk (J. Yang).

https://doi.org/10.1016/j.enggeo.2022.106594
Received 20 September 2021; Received in revised form 1 March 2022; Accepted 2 March 2022
Available online 5 March 2022

include field surveys, physical model tests, analytical and numerical calculations.

From field surveys perspective (including observation and monitoring), Davis and West (1973) recorded the aftershocks of the San Fernando earthquake as early as 1971 using strong-motion seismometers, and validated the amplification effect of the top relative to the foot by installing multiple stations on the slope surface. Long-term monitoring of a potential landslide by Del Gaudio and Wasowski (2007) indicated that the frequency band of energy distribution in the response spectrum is related to the slope orientation and incident direction of seismic waves, while topographic and geological conditions may lead to redistribution of energy. Following the 12 May 2008 Wenchuan M_S 8.0 earthquake, a greater interest in the dynamic response and instability mechanisms of slopes has been raised by earthquake geology researchers. Chigira et al. (2010) noted from field investigations that carbonate slopes with good stratification (easily dissolved by carbonates contained in groundwater) had the highest landslide risk in the Wenchuan earthquake, where the sliding surfaces were usually aligned along layer interfaces. Xu et al. (2009) and Zhi et al. (2015) showed that earthquake-induced slope instability is strongly dependent on topographic conditions based on field investigation and remote sensing interpretation of the 2008 Wenchuan earthquake and the 2013 Lushan earthquake. They also demonstrated that most of the geological hazards are concentrated in the slope angle range of $20^\circ \sim 50^\circ$, under which the earthquake ground motions exhibit a significant site amplification effect, with the top and protrusions of the slope being most prone to instability. Bolla and Paronuzzi (2020) presented a geomechanical study of a natural rock slope located in north-eastern Italy, and concluded that the duration of progressive slope failure is strongly dependent on the interaction of local geological factors (including lithology and tectonic) and seismic activity. From physical model tests perspective, Lin and Wang (2006) performed a large shaking model test to study the slope behavior under different seismic conditions, and indicated that the loading amplitudes below 0.4 g can remain linear while nonlinearity may occur for amplitudes above 0.5 g. Liu et al. (2013, 2014) further studied the influence of ground motion intensity and seismic parameters on acceleration amplification of rock slopes with the aid of shaking table tests. Yang et al. (2018) analyzed the seismic amplification and deformation characteristics of an anti-dip rock slope for different excitation frequencies by a large shaking table model. More follow-up studies could be found in the works of Zhu et al. (2020), Zhao et al. (2020), Chen et al. (2020). All the above studies are helpful for seismologists and geologists to gain some insightful understanding of regularities. However, due to too many factors affecting field monitoring and the lack of strong motion records, it is still difficult to accurately obtain the complete patterns of slope response from limited data so far. Also, although shaking table or other advanced testing techniques have been widely used in related studies, the conclusions presented may still be limited due to the limitations of size effect, gravity distortion, physical boundary conditions, material similarity ratio, and experimental expenses, resulting in test data that are not fully consistent with the actual case.

With the development of elastodynamic theory and computing technology, analytical and numerical calculations are extensively adopted to solve the dynamic problems of slope topography. The solution approaches include closed-form analytical scheme (e.g., wave function expansion method (Eshraghi and Dravinski, 1989), semi-analytical scheme relying on frequency-domain Green's function (e.g., boundary integral equation method (Bouchon and Sánchez-Sesma, 2007)), and various numerical schemes based on time-domain algorithms (e.g., finite element method (Huang et al., 2015), finite difference method (Xiao et al., 2016), and discrete element method (Lu et al., 2018)). Of the outstanding contributions in this subject, Zhang et al. (2017), and Liu et al. (2019) give the analytical expressions for the scattering of elastic waves by a slope or other simple geometries using the wave function expansion method, with the incident waves covering SH-, P-, SV-, and Rayleigh-waves. Bhasin and Kaynia (2004) used a discrete element method to analyze the static and dynamic characteristics of a 700-m high rock slope in western Norway, and their results showed that certain cumulative displacements are formed on the slope surface as the seismic loading holds. Zhang et al. (2015) studied the influence of vertical seismic force on the initiation mechanism of large-scale near-fault landslides by using the shear strength reduction technique combined with finite-difference modeling. Assefa et al. (2017) developed a distinct element model of Marly-Arenaceous formation with a regular layered structure and analyzed the displacement time-histories of a deep-seated slope movement in a complex rock. Fan et al. (2018b) proposed a seismic load input method accompanied by artificial viscous boundaries, and investigated the influence of the incident angle of seismic waves on the rock slope amplification coefficient using FLAC software. Song et al. (2020) proposed a joint time-frequency analysis method based on finite element technique, to investigate the effects of topographic and geological conditions on the seismic response of a bedding rock slope.

Existing studies have contributed significantly to the development of slope dynamics and geological engineering. Some consensus has been formed, though most of them are qualitative understanding, such as: (1) The earthquake ground motions of slopes show evident topographic site effect; (2) The acceleration responses of slopes are mainly in the horizontal direction, followed by vertical one; (3) The time-history characteristics of the slopes are strongly influenced by seismic source, propagation path, and topographic features. Nevertheless, in view of the complexity of rock slope dynamics, further exploration of wave propagation mechanism and quantitative parameter analysis of slope amplification effect is necessary. To this end, a semi-analytical method for solving in-plane elastic wave scattering by slope topography is presented to study the ground motion of rock slopes due to P and SV waves with an arbitrary incident angle. In this study, both the free- and scattered- wave fields are addressed directly from the wave equations, with no error accumulation in theory, so the presented solutions are accurate. Moreover, compared to the more studied case of out-of-plane SH wave incidence, the in-plane wave scattering problem is relatively rarely reported. This may be attributable to the challenges posed by the complex P/SV mode conversion and the zero-stress boundary condition along the half-space surface (Zhang et al., 2017). Therefore, this paper introduces a novel theoretical method to deal with engineering geological issues relevant to earthquakes, which can advance the understanding of the dynamic response of rock slopes under oblique incidence, and facilitate the evaluation of the sensitivity of slope seismic response to changes in incident wave frequency, incident angle and layering number. This study provides a physical interpretation of the amplification effect and distribution characteristics of earthquake-induced rock landslides, and reveals the dynamic mechanism of wave propagation and scattering by stratified rock slopes. To make the results more convincing, this paper endeavors to perform theoretical parametric analysis and practical case studies, which validate the feasibility of new method for engineering geologists to assess landslide hazards rapidly and preliminarily.

The paper is organized as follows: In Section 2, the theoretical formulations are introduced, including the free field solution based on the exact stiffness matrix and the scattered wave field solution based on dynamic Green's functions. In Section 3, the proposed methodology is implemented by the Fortran code, and is verified by comparing with the transfer matrix method. In Section 4, taking a rock slope site overlying bedrock half-space as an example, the seismic effects for different slope height, slope angle, shear velocity, and incident wave types are studied, and the results are analyzed in detail. In Section 5, sensitivity analyses of the semi-analytical approach are performed on model slopes with varying incident wave frequencies and incident angles. In Section 6, the semi-analytical approach is applied to a realistic case at Xishan slope in Zigong, China, which suffered extensive topography-induced damages in the 2008 Wenchuan earthquake. Section 7 presents a summary and draws some main conclusions.

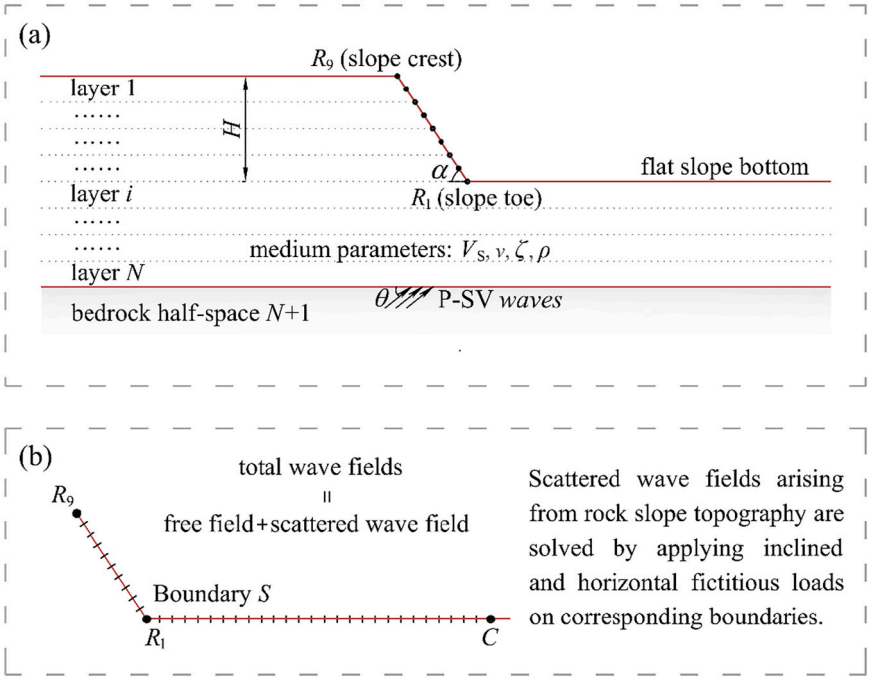

Fig. 1. Analytical model for dynamic response of a rock slope due to P and SV waves.

2. Theoretical formulations

2.1. Analytical model and method

The analytical model for dynamic response of a rock slope induced by P and SV waves with an arbitrary angle is shown in Fig. 1, with the height of H and slope angle of α ($0^\circ < \alpha \leq 90^\circ$), and both the slope and underlying medium can be horizontally stratified (where the sub-layers are numbered as i ($i = 1 \sim N$), and the bedrock half-space is numbered as $N + 1$). All material parameters include shear wave velocity V_S or elastic modulus E (where $E = \mu(1 + \nu)$, $G = \rho V_S^2$), Poisson's ratio ν, damping ratio ζ and mass density ρ. For the sake of conciseness, the elastic waves are assumed to be incident from the underlying bedrock with an incident angle of θ.

The solution of the analytical model is essentially the scattering and diffraction of seismic waves by slope topography. Mainly, the free boundary conditions (see Fig. 1b) are composed of a slope surface and a flat slope bottom (infinite extension), thus it can be simulated by using Green's function with the inclined and horizontal fictitious loads on corresponding boundaries, respectively.

It is worth stating that the infinite boundary here is different from the finite domain intercepted by using the finite element method. In this regard, we proposed a semi-analytical method depending on the integration over boundary elements, which has the merit of reducing dimension and automatically satisfying the infinity radiation condition compared with the finite element method. The key for resolving this time-domain dynamic problem is: (1) how to deal with the infinite boundary, and (2) how to discrete the boundary element as well as ensure the accuracy of the solution. In our method, the horizontal semi-infinite boundary is intercepted to point C on the premise of satisfying the precision, which can be determined by numerical trial calculations, as described in Section 3. Then, reasonable element division and suitable integral scheme setting should be determined to improve the computing efficiency as much as possible while ensuring the accuracy.

The analytical steps are as follows: (1) The total wave fields are decomposed into the free-field and scattered wave field; (2) The dynamic Green's functions are solved by applying the fictitious distributed loads on the corresponding boundaries to simulate the scattered wave field generated by slope topography, simultaneously, the free field can be conveniently modeled by the direct stiffness method. (3) The zero-stress boundary conditions of free surface are introduced to determine the fictitious loads, and then the scattering wave field can be determined, and finally the total responses are derived by superposition. The total displacement vector $\mathbf{u}$ can be expressed as

$$(\lambda+\mu)\nabla\nabla\mathbf{u}+\mu\Delta\mathbf{u} = -\rho\omega^2\mathbf{u} \tag{1}$$

where $\boldsymbol{u}$ denote the displacement vector at an arbitrary point of slope model; λ and μ are two Lamé's constants; ∇ and $\Delta = \nabla\cdot\nabla$ are the Nabla operator and Laplace operator, respectively. Based on the concept of wave field separation, the total displacement can be divided into free-field one and scattered wave field one as follows:

$$u_i = u_i^f + u_i^s \qquad (i = x, z) \tag{2}$$

2.2. Free field

The free-field response of stratified media is a fundamental issue for studying wave propagation and dynamic soil-structure interaction, which has been tackled by many scholars using different methods (Thomson, 1950; Haskell, 1953; Kausel and Roësset, 1981; Wolf and Obernhuber, 1982; Yang, 2002). By using the dynamic stiffness matrix (Yang and Yan, 2009a, 2009b), the free field can be obtained by solving Eq. (3)

$$\mathbf{Q} = \mathbf{S}_{\text{P-SV}}\mathbf{U} \tag{3}$$

where $\mathbf{S}_{\text{P-SV}}$ is the global dynamical stiffness matrix of layered half-space, which can be determined by assembling the layer stiffness matrix $\mathbf{S}^{\text{L}}_{\text{P-SV}}$ and the half-space one $\mathbf{S}^{\text{R}}_{\text{P-SV}}$, and the subvectors of these matrices can be found in Wolf and Obernhuber (1982). $\mathbf{Q} = \{P_1, \mathrm{i}R_1, P_2, \mathrm{i}R_2, \cdots, P_{N+1}, \mathrm{i}R_{N+1}\}^{\text{T}}$ is the vector consisting of the external load amplitudes at layer interfaces, and $\mathbf{U} = \{u_1, \mathrm{i}w_1, u_2, \mathrm{i}w_2, \cdots, u_{N+1}, \mathrm{i}w_{N+1}\}^{\text{T}}$ is the corresponding displacement amplitude vector. When the control point is selected at an assumed rock outcrop, the last two parameters can be determined by Eq. (4), while the remaining parameters should be equal to zero.

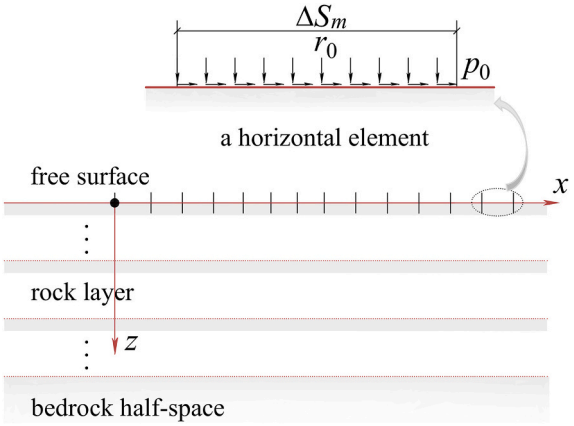

Fig. 2. Sketch of Green's functions for horizontal distributed loads.

$$\begin{Bmatrix} P_0 \\ \mathrm{i}R_0 \end{Bmatrix} = \mathbf{S}^{\mathrm{R}}_{\mathrm{P\text{-}SV}} \begin{Bmatrix} u_{x,0} \\ u_{z,0} \end{Bmatrix} \tag{4}$$

where P_0 and R_0 are the load amplitudes of bedrock motion in the x and z directions respectively, and $u_{x,0}$ and $u_{z,0}$ are the corresponding displacement amplitudes. Substituting Eq. (4) into Eq. (3), the displacement amplitudes at layer interfaces are obtained, and then the displacement u_i^f, and traction t_i^fat an arbitrary point on the free boundaries can be calculated.

2.3. Scattered wave field

In the wavenumber-based method, the scattered wave field can be simulated by applying the fictitious distributed or point loads on the free boundary and soil structure interface (Beskos, 1987). In the slope model, the entire boundary is assumed to be $S{=}S_1 + S_2$, with S_1 denoting the slope surface and S_2 denoting the flat slope bottom. The boundary S_1 is discretized into a finite number of K_1 line elements, each with a width of $\Delta S_l (l \in [1, K_1])$. However, the boundary S_2 has a theoretically infinite number of line elements, thus a truncation point C is introduced to allow for an analytic representation. Also, the intercepted new boundary S_2 is discretized into a finite number of K_2 line elements with the width of $\Delta S_m (m \in [1, K_2])$. As a result, the displacement and traction amplitudes caused by the scattered wave field of rock slope can be formulated as

$$\begin{aligned} u_i^t(\mathbf{x}) &= u_i^{s_1}(\mathbf{x}) + u_i^{s_2}(\mathbf{x}) \\ &= \sum_{l=1}^{K_1} u_{ij}(\mathbf{x}, \xi_l)\phi_j(\xi_l) + \sum_{m=1}^{K_2} u_{ij}(\mathbf{x}, \xi_m)\phi_j(\xi_m), (i,j = x,z) \end{aligned} \tag{5}$$

$$\begin{aligned} t_i^t(\mathbf{x}) &= t_i^{s_1}(\mathbf{x}) + t_i^{s_2}(\mathbf{x}) \\ &= \sum_{l=1}^{K_1} t_{ij}(\mathbf{x}, \xi_l)\phi_j(\xi_l) + \sum_{m=1}^{K_2} t_{ij}(\mathbf{x}, \xi_m)\phi_j(\xi_m)\,, (i,j = x,z) \end{aligned} \tag{6}$$

where the superscript "t" indicates the total scattered wave field. $u_{ij}(\mathbf{x}, \xi_l)$ and $t_{ij}(\mathbf{x}, \xi_l)$ are half-space Green's functions for displacement and traction of the inclined distributed loads, and $u_{ij}(\mathbf{x}, \xi_m)$ and $t_{ij}(\mathbf{x}, \xi_m)$ are half-space Green's functions for displacement and traction of the horizontal distributed loads.

Evidently, we should deal with two types of Green's functions, which are not constructed in exactly the same way. For the inclined line type, Wolf's theory (Wolf, 1985) can be applied to the formula. For the horizontal line type, since the solution process is independent of the fixed layer interface (the aim is to calculate the particular solution and homogeneous solution), the line loads are applied directly on the horizontal boundary and then the dynamic response can be easily obtained by using the direct stiffness method (Kausel and Roësset, 1981; Degrande, 2002). The two types of half-space dynamic Green's functions are described as follows.

1. Green's functions for inclined distributed loads

It is worth stating that for observations located within the fixed layer, the responses contain the particular, homogeneous and reaction solutions; while for other layer's observations, only the reaction solution is required. Thus, when $\mathbf{x}$ is a fixed layer point, the dynamic Green's functions can be written as

$$u_{ij}(\mathbf{x}, \xi_l) = \int_{-\infty}^{\infty} \left[u_{ij}^{\mathrm{p}}(\mathbf{x}, \xi_l, k) + u_{ij}^{\mathrm{h}}(\mathbf{x}, \xi_l, k) + u_{ij}^{\mathrm{r}}(\mathbf{x}, \xi_l, k) \right] e^{-\mathrm{i}kx} dk \tag{7}$$

$$t_{ij}(\mathbf{x}, \xi_l) = \int_{-\infty}^{\infty} \left[t_{ij}^{\mathrm{p}}(\mathbf{x}, \xi_l, k) + t_{ij}^{\mathrm{h}}(\mathbf{x}, \xi_l, k) + t_{ij}^{\mathrm{r}}(\mathbf{x}, \xi_l, k) \right] e^{-\mathrm{i}kx} dk \tag{8}$$

when $\mathbf{x}$ is a non-fixed layer point, the dynamic Green's functions are

$$u_{ij}(\mathbf{x}, \xi_l) = \int_{-\infty}^{\infty} \left[u_{ij}^{\mathrm{r}}(\mathbf{x}, \xi_l, k) \right] e^{-\mathrm{i}kx} dk \tag{9}$$

$$t_{ij}(\mathbf{x}, \xi_l) = \int_{-\infty}^{\infty} \left[t_{ij}^{\mathrm{r}}(\mathbf{x}, \xi_l, k) \right] e^{-\mathrm{i}kx} dk \tag{10}$$

The superscript "p" denotes the particular solution in the fixed layer, the superscript "h" denotes the homogeneous solution in the fixed layer, the superscript "r" denotes the reaction solution, and k is the horizontal wavenumber. A more detailed description with respect to the "fixed layer" can be found in Wolf (1985).

2. Green's functions for horizontal distributed loads

The general process can be summarized as follows: first, the fictitious distributed loads are expanded from space domain to wavenumber domain by Fourier transform; then, by applying the distributed loads directly at the horizontal elements, the response generated by these loads is calculated with the aid of dynamic stiffness matrix; finally, the steady-state solution in the space domain is obtained by inverse Fourier transform.

For the fictitious distributed loads applied on the horizontal element with a width of ΔS_{m} shown in Fig. 2, the amplitudes in the x and z directions are assumed to be p_0 and r_0, respectively. These loads can be expanded in the wavenumber domain as

$$p(k,0) = \frac{p_0}{2\pi} \int_0^{\Delta S_m} exp(\mathrm{i}kx)\mathrm{d}x = -\frac{\mathrm{i}p_0}{2\pi k}[exp(\mathrm{i}k\Delta S_m) - 1] \tag{11}$$

$$r(k,0) = \frac{r_0}{2\pi} \int_0^{\Delta S_m} exp(\mathrm{i}kx)\mathrm{d}x = -\frac{\mathrm{i}r_0}{2\pi k}[exp(\mathrm{i}k\Delta S_m) - 1] \tag{12}$$

The corresponding displacement amplitudes can be determined by using global dynamical stiffness matrix

$$\mathbf{S}_{\mathrm{P\text{-}SV}} \left\{ u_{x1}, \mathrm{i}u_{z1}, \cdots, u_{x(N+1)}, \mathrm{i}u_{x(N+1)} \right\}^{\mathrm{T}} = \{P_1, \mathrm{i}R_1, 0, \cdots, 0\}^{\mathrm{T}} \tag{13}$$

where $P_1 = p(k)$ and $R_1 = r(k)$. Then, combining the following stress-displacement relationship, the stresses due to fictitious loads can be further derived.

$$\sigma_x(k,z) = \lambda^* \left(\frac{\partial u_x}{\partial x} + \frac{\partial u_z}{\partial z} \right) + 2\mu^* \frac{\partial u_x}{\partial x} \tag{14}$$

$$\sigma_z(k,z) = \lambda^* \left(\frac{\partial u_x}{\partial x} + \frac{\partial u_z}{\partial z} \right) + 2\mu^* \frac{\partial u_z}{\partial z} \tag{15}$$

$$\tau_{xz}(k,z) = \mu^* \left(\frac{\partial u_x}{\partial z} + \frac{\partial u_z}{\partial x} \right) \tag{16}$$

Performing the inverse Fourier transform, the half-space Green's functions for displacement and traction under the horizontal line loads

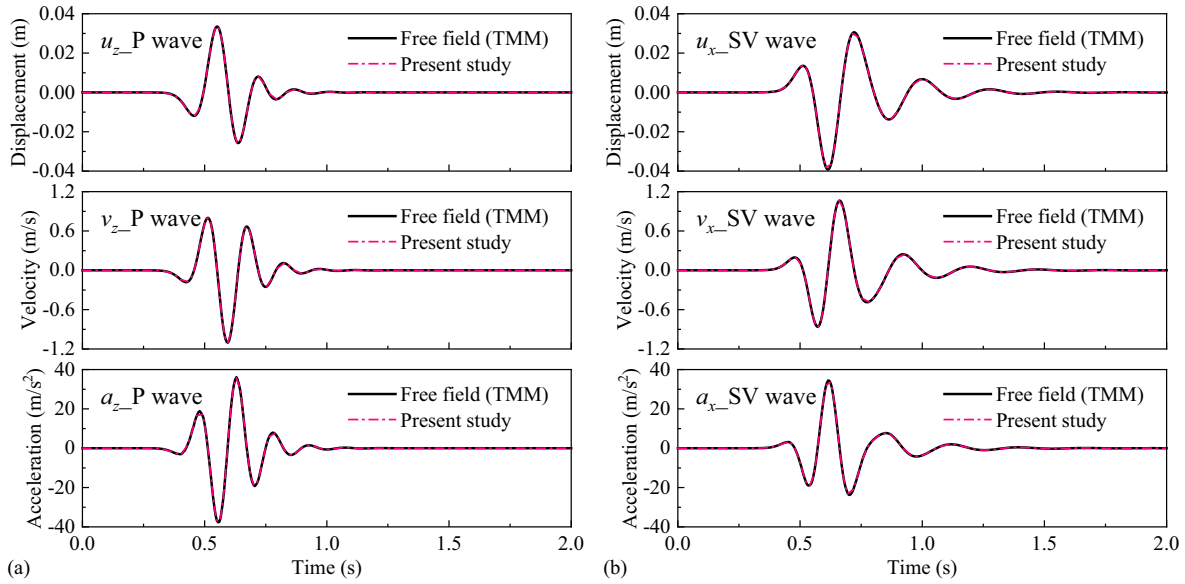

Fig. 3. Comparison of time-history curves for displacement, velocity and acceleration of the site surface to vertically incident P and SV waves using transfer matrix method (TMM, solid black line) and present method (dotted dash line). (a) Vertical ground motion due to P waves; (b) Horizontal ground motion due to SV waves.

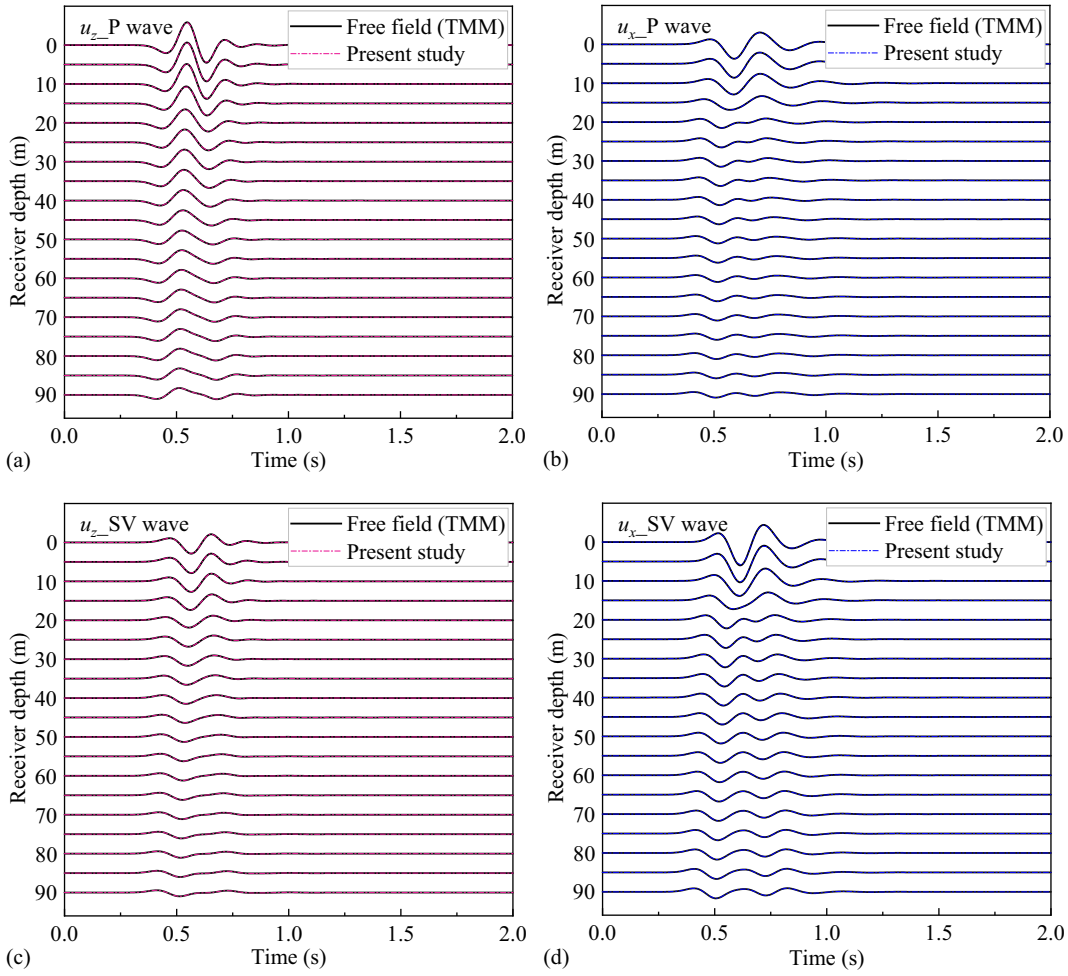

Fig. 4. Comparison of displacement seismograms distributed along the site depth to obliquely incident P and SV waves using transfer matrix method (TMM, solid black line) and present method (dotted dash line). (a) Vertical displacement due to P waves; (b) Horizontal displacement due to P waves; (c) Vertical displacement due to SV waves; (d) Horizontal displacement due to SV waves.

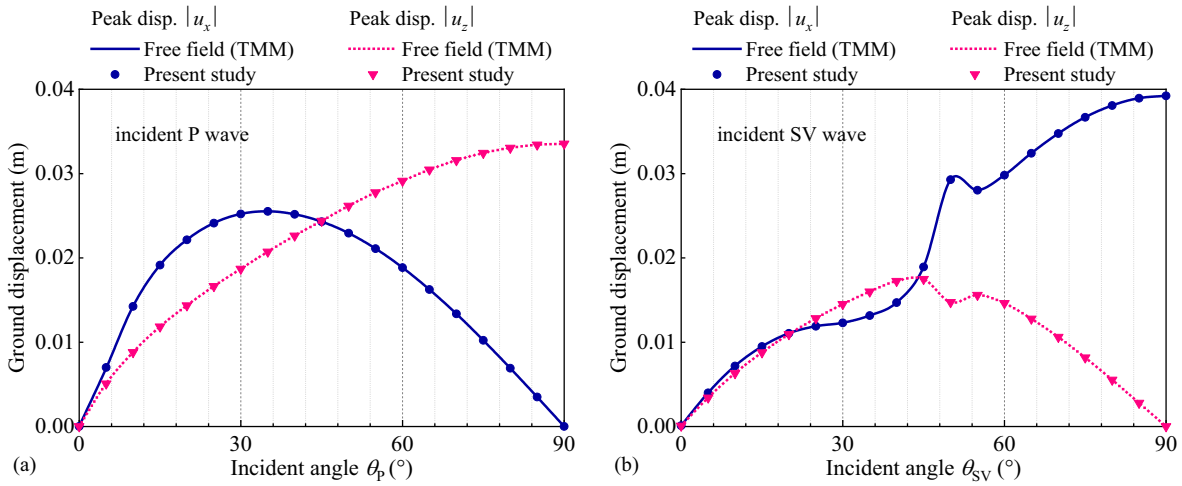

Fig. 5. Comparison of ground displacement of a stratified site subjected to obliquely P and SV waves with arbitrary incident angles. (a) Relationship between the angle θ_P of P-wave and peak ground displacement; (b) Relationship between the angle θ_{SV} of SV-wave and peak ground displacement.

are

$$u_{ij}(x,z) = \int_{-\infty}^{\infty} u_{ij}(k,z)exp(-\mathrm{i}kx)\mathrm{d}k, (i,j = x,z) \tag{17}$$

$$t_{ij}(x,z) = \int_{-\infty}^{\infty} t_{ij}(k,z)exp(-\mathrm{i}kx)\mathrm{d}k, (i,j = x,z) \tag{18}$$

In Eq. (18), the traction component can be obtained by the projection of stresses.

$$t_{xj}(k,z) = n_x\sigma_x(k,z) + n_z\tau_{xz}(k,z) \tag{19}$$

$$t_{zj}(k,z) = n_x\tau_{zx}(k,z) + n_z\sigma_z(k,z) \tag{20}$$

where $\mathbf{n} = (n_x, n_z)$ is the normal vector for point **x**.

2.4. Boundary conditions

The zero-traction condition on the boundary S of the slope model can be formulated from Eq. (21), and the integral can be evaluated separately over each element.

$$\int_S \left[t_i^t(\boldsymbol{x}_n) + t_i^f(\boldsymbol{x}_n)\right]\mathrm{d}S = 0 \ (i = x,z) \tag{21}$$

where subscript n is the total number of discretized boundary elements.

It is noted that the above derivations are performed in the frequency domain, whereas the time-history response of a stratified rock slope subjected to incident seismic waves is determined by superimposing the frequency-domain solution:

$$\mathbf{u}(x,z,t) = \int_{-\infty}^{+\infty} u_{ij}(x,z,\omega)\mathrm{e}^{\mathrm{i}\omega t}\mathrm{d}\omega \tag{22}$$

$$\mathbf{v}(x,z,t) = (\mathrm{i}\omega)\cdot\int_{-\infty}^{+\infty} u_{ij}(x,z,\omega)\mathrm{e}^{\mathrm{i}\omega t}\mathrm{d}\omega \tag{23}$$

$$\mathbf{a}(x,z,t) = \left(-\omega^2\right)\cdot\int_{-\infty}^{+\infty} u_{ij}(x,z,\omega)\mathrm{e}^{\mathrm{i}\omega t}\mathrm{d}\omega \tag{24}$$

where $\boldsymbol{u}$, $\boldsymbol{v}$ and $\boldsymbol{a}$ correspond to the displacement, velocity and acceleration vectors in the time-domain solution, respectively.

3. Verification and convergence

3.1. Accuracy verification of the method: vertically incident waves

As shown in Fig. 1, for a special slope with $\theta = 90°$, its dynamic response under seismic excitation can be regarded as free field motion. As a result, the correctness of the proposed method can be verified by comparing with the classical transfer matrix method (TMM, Thomson, 1950; Haskell, 1953) to calculate the surface response of layered sites. In the calculation, a horizontal layered slope is composed of three rock layers of different geological materials with the parameters characterized as follows: layer thickness $d_1 = 20$ m, $d_2 = 30$ m, $d_3 = 40$ m; shear velocity $V_{S,1} = 350$ m/s, $V_{S,2} = 900$ m/s, $V_{S,3} = 1600$ m/s; Poisson's ratio $\nu_1 = 0.32$, $\nu_2 = 0.27$, $\nu_3 = 0.23$; mass density $\rho_1 = 2300$ kg/m^3, $\rho_2 = 2500$ kg/m^3, $\rho_3 = 2700$ kg/m^3; material damping ζ_1=ζ_2=ζ_3= 0.05, where the subscript 1–3 represent the layer number, and the parameters of the bedrock half-space are consistent with those of layer 3. A Ricker wavelet with displacement function of $u(t) = A \cdot [2\pi^2 f_{02}(t-0.5)^2 - 1]\, e^{-\pi 2 f_{02}(t-0.5)2}$ is used as the input, where the amplitude of wavelet is A = 0.01 m and the center frequency is $f_0 = 4.0$ Hz. The time-history curves for surface displacement, velocity and acceleration of the sites to vertically incident P and SV waves are shown in Fig. 3, from which the excellent agreement shows the capability of our method.

3.2. Accuracy verification of the method: obliquely incident waves

To verify the correctness for obliquely incident P and SV waves, the above special model with stratified characteristics is still considered, and only the incident angle is replaced by $\theta = 60°$. Note that in contrast to the vertically incident case, the horizontal and vertical components of ground motion are expected to be valued for obliquely incident seismic waves. For adequate comparison, multiple receivers are arranged along the depth direction from 0 to 90 m with the coordinate origin (0,0), and the recorded displacement seismograms in two directions of the sites are depicted in Fig. 4. It can be seen that all displacement components calculated from our method match those obtained with TMM.

Furthermore, a comparison of ground displacement of a stratified site subjected to obliquely P and SV waves with arbitrary incident angles is presented. As illustrated in Fig. 5, the subplots from left to right are the relationships of the angle θ_P of P-wave angle θ_{SV} of SV-wave with peak ground displacement, respectively. Comparisons of the Horizontal and vertical responses shown in Fig. 5 confirm the accuracy of the present results again.

Table 1
Convergence analysis of the method for different incident frequencies.

Receiver position	$f = 2.0$ Hz										
	$D = 1.0\lambda$	$D = 2.0\lambda$	$D = 3.0\lambda$	$D = 4.0\lambda$	$D = 5.0\lambda$	$D = 6.0\lambda$	$D = 7.0\lambda$	$D = 8.0\lambda$	$D = 9.0\lambda$	$D = 10.0\lambda$	$D = 11.0\lambda$	$D = 12.0\lambda$
crest	7.0503	6.7110	6.0265	6.6960	6.9795	6.4222	6.2615	6.1957	6.2290	6.2479	6.2525	6.2307
waist	5.3187	5.0577	4.3853	4.5331	5.2748	5.0223	4.7859	4.6529	4.6778	4.6854	4.6975	4.6900
toe	1.2913	1.1612	0.9819	1.2040	1.1419	1.1010	1.0990	1.0895	1.0850	1.0824	1.0874	1.0868
Receiver position	$f = 12.0$ Hz											
	$D = 1.0\lambda$	$D = 2.0\lambda$	$D = 3.0\lambda$	$D = 4.0\lambda$	$D = 5.0\lambda$	$D = 6.0\lambda$	$D = 7.0\lambda$	$D = 8.0\lambda$	$D = 9.0\lambda$	$D = 10.0\lambda$	$D = 11.0\lambda$	$D = 12.0\lambda$
crest	3.1715	3.2221	3.3941	3.4403	3.2040	3.2428	3.2889	3.2728	3.264	3.2688	3.2704	3.2747
waist	2.1475	2.1564	2.276	2.3052	2.2140	2.1585	2.2013	2.2154	2.2123	2.2228	2.2297	2.2200
toe	1.8457	1.883	1.8667	1.9699	2.0588	2.0143	1.9253	1.9299	1.9372	1.9432	1.9404	1.9386

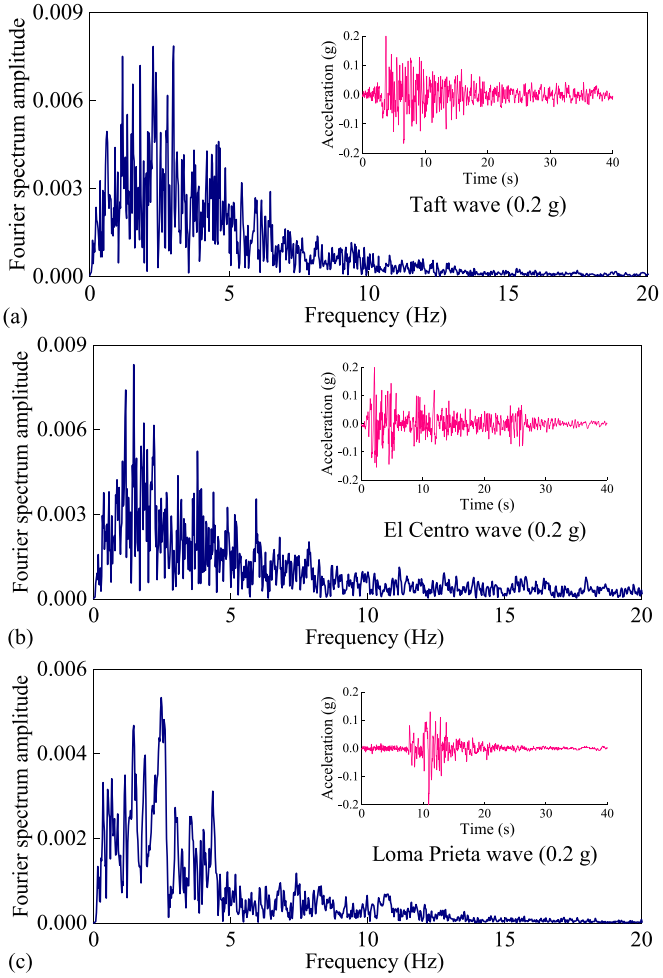

Fig. 6. Fourier spectrum characteristics for seismic inputs. (a) Taft wave; (b) El Centro wave; (c) Loma Prieta wave.

Table 2
The setting of slope characteristics and seismic input.

Number	Parameters	Values
①	Slope height H/m	15 , 30 , 50 , 80
②	Slope angle α/(°)	14 , 28 , 42 , 56 , 70
③	Rock mass	I ~ V level
④	Seismic input	Taft wave (0.2 g), El Centro wave (0.2 g), Loma Prieta wave (0.2 g)

Table 3
Material parameters for rock slopes with different strength levels.

Strength level		Shear velocity V_S (m/s)	Poisson's ratio ν	Density ρ (kg/m^3)
Harder rock slope (I ~ II level)	I	2500 2350	0.27	2500
	II	2200 1900	0.27	2500
Softer rock slope (III ~ V level)	III	1600 1250	0.27	2500
	IV	900 700	0.27	2500
	V	450 350	0.27	2500

Note: For all slope materials, the damping ratio is $\zeta = 0.02$.

3.3. Convergence analysis of the method

The methodology presented in this paper is implemented by the Fortran program, which can be easily combined with the high-performance OpenMP parallel technique (Chandra et al., 2001). As a result, the precision and efficiency of the algorithm are closely related to the convergence of the solution as well as the wavenumber integration scheme. To this end, a trial calculation analysis of rock slope with $\alpha = 70°$ was carried out, where other parameters in accordance with Section 3.1. The variation of the surface displacement amplitude with the truncation distance D_{max} for several representative observation points at two incident frequencies is given in Table 1. It shows that with the increase of D_{max}, the solution tends to be stable, and good convergence is observed in both low and high frequencies. When D_{max} exceeds 8 times the wavelength λ, the amplitude fluctuations of surface displacements are already quite slight. In the subsequent study, $D_{max} = 10\lambda$ is adopted to satisfy the precision requirement. Additionally, for the numerical integration from the wavenumber domain to the space domain, a two-point Gaussian integral technique is employed regarding the oscillations of Bessel functions. After trial calculations, the maximum integral wavenumber segment is taken as $k_{max} = 200$–500, and each integral interval is taken as $\Delta k = 0.001$–0.002, to ensure stability in the calculation.

4. Parametric studies and analysis

4.1. Rock slope setting

To investigate the seismic response of rock slopes under actual seismic excitations, three earthquake records, namely Taft wave, El Centro wave and Loma Prieta wave, are selected. The underlying bedrock is assumed to be elastic half-space with $V_S = 3500$ m/s, $\rho = 2650$ kg/m^3, $\nu = 0.2$ and $\zeta = 0.02$, and a vertical incident angle is considered. For the sake of comparison, the excitation intensity of all selected seismic shear waves is taken to be 0.2 g, with a duration of 40 s, and the corresponding Fourier spectrum characteristics are shown in Fig. 6.

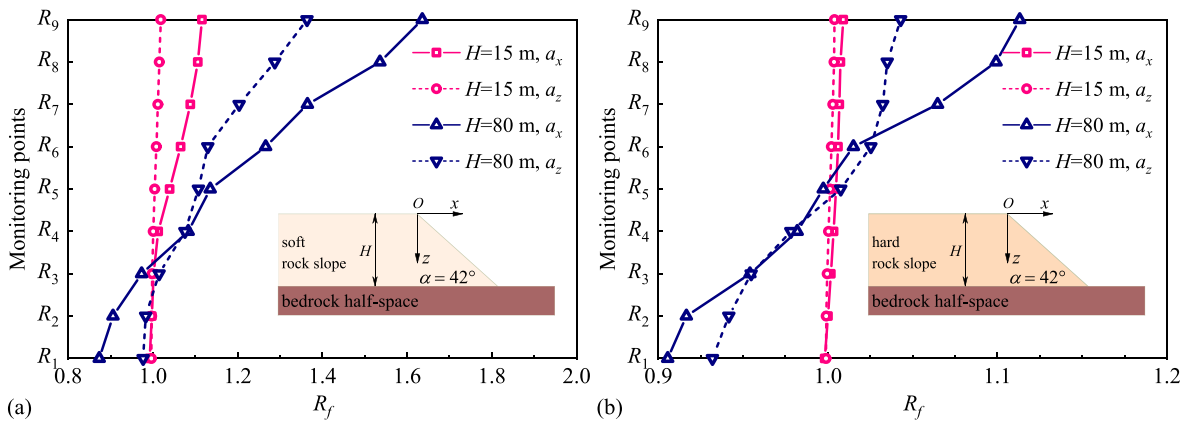

Fig. 7. Horizontal and vertical acceleration responses of rock slopes with different slope heights. (a) for soft rock slope; (b) for hard rock slope.

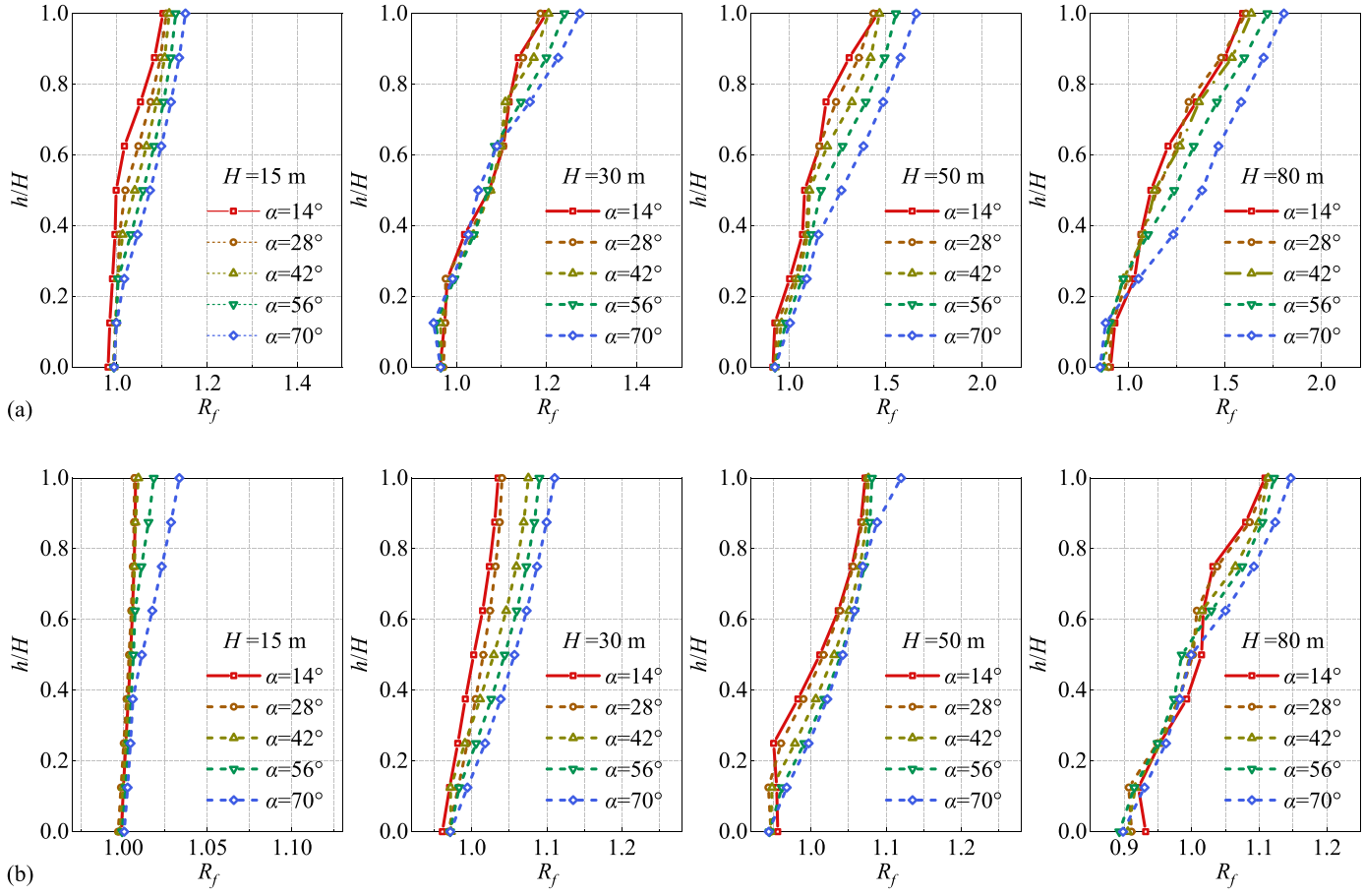

Fig. 8. PGA amplification factor of slope surface versus relative elevation for different geometric parameters. (a) for soft rock slope; (b) for hard rock slope.

It is well established that the site effect of rock slopes (containing the topographic amplification effect and the stratigraphic amplification effect) is influenced by different conditions and numerous factors. In this section, two key affecting factors, the slope geometry parameters and shear velocity, are selected for analysis. First, the influence of geometric parameters on the dynamic response of rock slopes is studied, specifically considering different slope heights H and slope angles α (see Table 2). Next, the effect of shear velocity on the seismic response is investigated while keeping the slope geometric parameters at constant values ($H = 80$ m, $\alpha = 70°$). The lithology of rock slope is classified as I ~ V levels according to the rock quality index, and two sets of representative material parameters are selected for each level. It is noteworthy that the material parameters here only consider the variation of shear wave velocity to facilitate the comparative analysis of the results, and the rest of the parameters are taken as mean values, as shown in Table 3. In addition, multiple monitoring points $R_1 \sim R_9$ (see Fig. 1) are arranged on the slope surface with the relative elevations of $h/H = 0.0$, 0.125, 0.25, 0.375, 0.5, 0.625, 0.75, 0.875 and 1.0.

4.2. Dynamic characteristics of rock slope

4.2.1. Comparison of horizontal and vertical responses

The calculation results show that the slope responses for different seismic inputs share a similar pattern. Due to the limitation of space, this

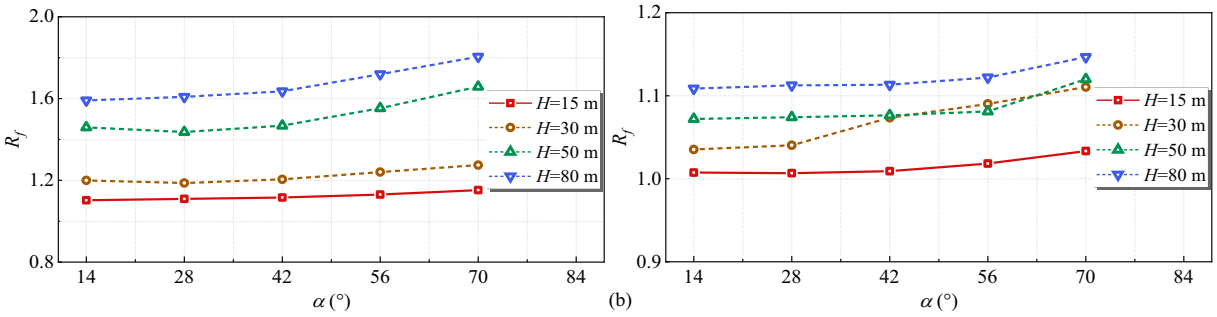

Fig. 9. The variation of PGA amplification factor at slope crest with geometric angle. (a) for soft rock slope; (b) for hard rock slope.

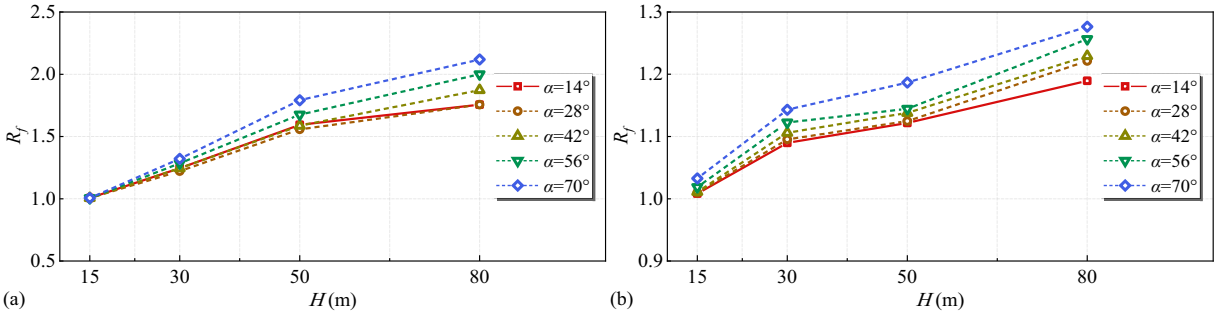

Fig. 10. The variation of PGA amplification factor at slope crest with slope height. (a) for soft rock slope; (b) for hard rock slope.

section takes the Taft wave as an example for analysis. First of all, the amplification factor (R_f) of peak ground acceleration (PGA) is introduced to reflect the site effect of rock slope, which is defined as

$$R_f = \frac{PGA(m)}{PGA(0)} \tag{25}$$

where $PGA(m)$ is the PGA of monitoring point m (m = 1–9) on the slope surface, and $PGA(0)$ is the PGA of free-field response, i.e., the reference response is assumed to the free-field motion of flat slope bottom.

The comparison results of horizontal and vertical acceleration responses of rock slopes with different slope heights at the same slope angle ($\alpha = 42°$ as an example) are shown in Fig. 7. The horizontal component of acceleration response due to incident seismic shear waves is significantly stronger than the vertical one for both soft and hard rocks, which is consistent with the analysis of existing studies (Lin and Wang, 2006; Liu et al., 2013, 2014). An extensive statistics of example studies (different incident wave types, lithology and geometric parameters) draws the following conclusions: Under the given parameter setting in this work, the horizontal R_f is 1.03–1.56 times higher than the vertical one for the soft rock case. While for the hard rock case, the R_f in the horizontal direction is 1.0 to 1.16 times that in the vertical direction. For convenience, the horizontal amplification effect is mainly discussed later.

4.2.2. Effect of slope geometry on seismic response

Fig. 8 shows the variation of R_f of slope surface with relative elevation for different geometric parameters. A significant elevation amplification effect is observed in the acceleration response of rock slope. As the relative elevation increases, the amplification curves present a nonlinear increasing trend, and the maximum peak almost always occurs at the crest of the slope. Moreover, the elevation amplification effect is mainly concentrated in the middle and upper parts of the slope. For example, when $h/H < 0.3$, the amplification of slope acceleration is less obvious, while when $h/H \geq 0.3$, this amplification effect is significant with a rapid change of R_f.

On the other hand, a de-amplification phenomenon exists in the dynamic response near the slope toe. This is due to the interaction of the upper protruding topography with the lower bedrock half-space, which alters the dynamic characteristics of the local rock site, resulting in slightly smaller amplitudes at the toe and lower part of the slope than on the flat slope bottom (the response of flat bottom away from the slope is equivalent to free field motion). Alternatively, this interesting result may also be due to the differences in the bedrock/slope properties that allow the horizontal ground motion to be de-amplified at the toe of the slope, and this overestimation may be stronger for steeper slopes. Similar discussions and analyses can be found in numerical studies and field measurements (without appropriate free field selection), see Bouckovalas and Papadimitriou (2005). This reminds relevant researchers that once the reference site in the definition of amplification factor (see Eq. (25)) is taken at the slope toe, the overall amplification effect may be seriously overestimated.

The relationship between amplification factor at slope crest and geometric angle as well as height is further given in Fig. 9 and Fig. 10, respectively. In general, the angle and height of rock slope have essential impacts on the seismic response. The site effects of slopes for different lithology follow a similar profile, and the amplification is more pronounced for a soft rock slope. With the increase of slope angle, the R_f shows a tendency to increase. However, the amplification effect is not apparent in the small angle range, e.g., the factor value for $\alpha = 14°$ is slightly larger than that of $\alpha = 28°$, and only the factor value for slope height of 80 m increases significantly with the increase of slope angle. This reflects a strong nonlinear characteristic of the dynamic response of rock slope, yet the increase in slope angle can still be regarded as a positive contribution to the overall amplification effect. Besides, with the increase of slope height, the R_f also increases gradually. For slopes height lower than 50 m, the factor values increase rapidly with increasing slope height, while for slopes higher than 50 m, the increasing trend of factor values diminishes. This indicates that the dynamic response of slope may not always increase with increasing slope height. Since the dynamic response of a rock slope is influenced by a variety of factors (e.g., natural frequency and excitation intensity of ground motion), this subject will be continuously deepened in

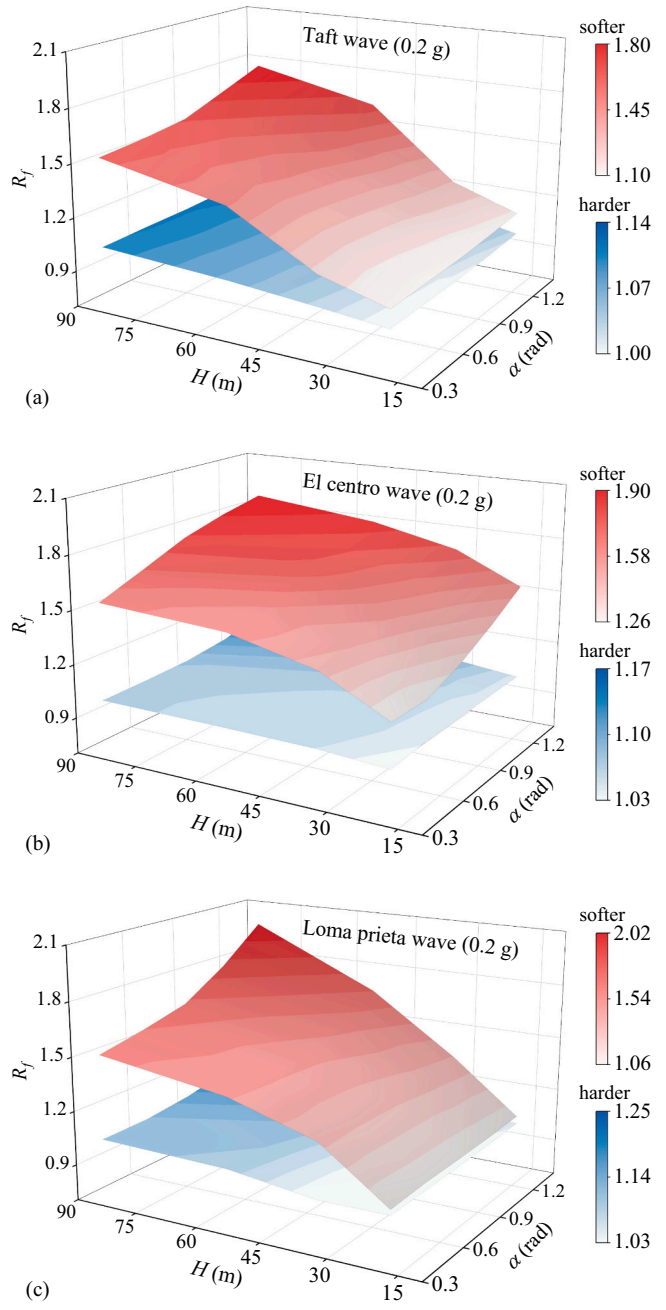

Fig. 11. PGA amplification factor in a three-dimensional space varying with geometrical parameters. (a) Taft wave; (b) El Centro wave; (c) Loma Prieta wave.

subsequent studies.

The above analysis reveals some fundamental regularities in the dynamic response of rock slopes. To provide a better reference for the seismic design of engineering slopes, the following quantitative results of the ground motion of slope crest are given via the fitting method. Fig. 11 depicts the amplification factor in a three-dimensional space varying with geometrical parameters, where the angle unit is converted from the angular to radian system. It shows that the influence of geometric parameters on ground motion amplification for different incident seismic waves is similar. Hence, taking slope height H and slope angle α as independent variables and amplification factor R_f for the slope crest as a dependent variable, the following expression is proposed as an empirical formula for the seismic response.

$$R_f = r_0 + r_1 H + r_2 \alpha + r_3 \alpha^2 + r_4 H\alpha \tag{26}$$

The coefficients to be solved in Eq. (26) are r_0, r_1, r_2, r_3 and r_4. According to the fitting results, the corresponding fitting parameters are shown in Table 4. Using the averages under different seismic as the recommended parameters, the fitted surface for the influence of

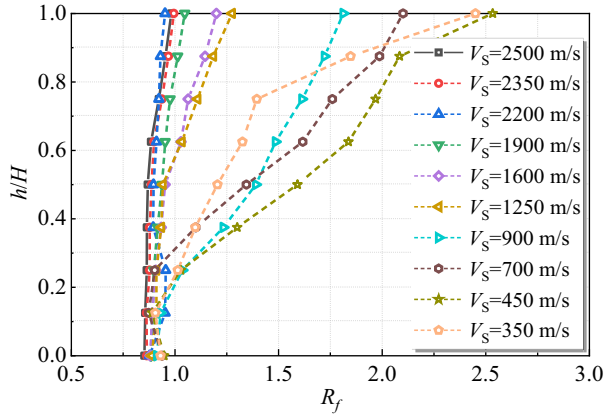

Fig. 12. PGA amplification factor of slope surface versus relative elevation for different shear velocities.

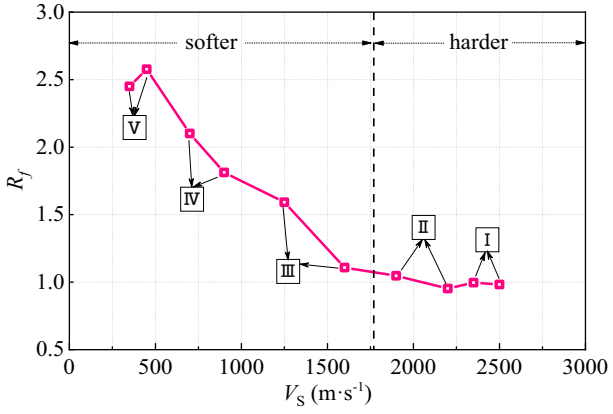

Fig. 13. The variation of PGA amplification factor at slope crest with shear velocity.

Table 4
Fitting results for the relationship between geometric parameters and amplification factor.

Fitting parameters	Fitted values for soft rock slope				Fitted values for hard rock slope			
	El.	Taft.	Loma.	Average	El.	Taft.	Loma.	Average
r_0	0.993	1.080	1.089	1.054	0.969	1.054	1.029	1.018
r_1	0.007	0.006	0.005	0.006	0.002	0.000	0.000	0.001
r_2	−0.272	0.175	−0.451	−0.183	−0.021	−0.090	−0.112	−0.074
r_3	0.186	0.080	0.225	0.164	0.048	0.058	0.071	0.059
r_4	0.003	0.000	0.006	0.003	0.000	0.001	0.002	0.001

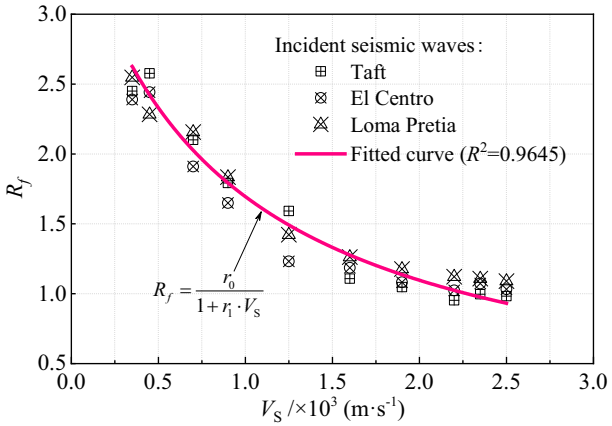

Fig. 14. Fitted curves for the influence of shear velocity on the PGA amplification factor.

geometric parameters on the amplification factor can be formulated as: $R_f = 1.054 + 0.006H - 0.183\alpha + 0.164\alpha^2 + 0.003H\alpha$ for soft rock slope, and $R_f = 1.018 + 0.001H - 0.074\alpha + 0.059\alpha^2 + 0.001H\alpha$ for hard rock slope. For a slope topographic feature similar to the one studied in this paper and the medium is homogeneous and isotropic, the empirical formula is worth generalizing.

4.2.3. *Effect of shear velocity on seismic response*

Taking the Taft wave as an example, the variation of R_f on slope surface with relative elevation for different shear velocities is shown in Fig. 12. It is evident that the seismic response of rock slope is highly influenced by shear velocity, which is embodied in two stages. At the stage of $V_S \geq 900$ m/s, the nonlinear features of PGA variation are weak with the increase of relative elevation, and the elevation effect is concentrated in the upper part of the slope surface. At the stage of $V_S < 900$ m/s, the nonlinear features of PGA variation are apparent with the increase of relative elevation. For a lower height, the amplification factor is slightly less than 1.0, which implies no amplification. With increasing relative elevation, the amplification factor increases rapidly and reaches a peak at slope crest. It should be noted that the engineering properties of soft rock slopes with $V_S < 900$ m/s are characterized by low strength, easy softening and weak stability. Thus, special attention should be paid to the potential damage of such slopes in engineering practice and standardization.

The relationship of amplification factor at slope crest and shear velocity is further illustrated in Fig. 13. With the increase of shear velocity, the curves share a decreasing trend. The maximum difference of factor values for the same lithology is nearly 2.7 times due to the effect of shear velocity, which indicates that the stratified amplification effect of the slope overlying bedrock half-space is remarkable. Moreover, the attenuation of R_f for soft rock slope is more evident than that for hard one. Based on the classification, the attenuation stages are mainly focused on III and IV levels, so the seismic response of these two types of slopes may be exclusively analyzed in subsequent works.

Fig. 14 plots the amplification factor varying with shear velocity for different incident seismic waves. According to the varying features of data points within the given range of shear velocity, taking shear

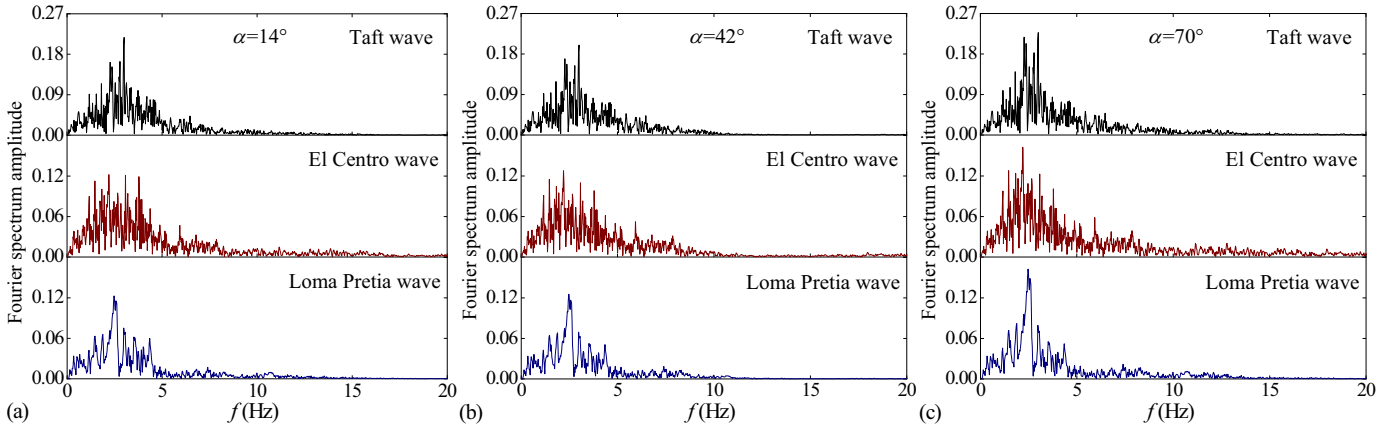

Fig. 15. Fourier amplitude spectra of rock slopes with different geometric angles.

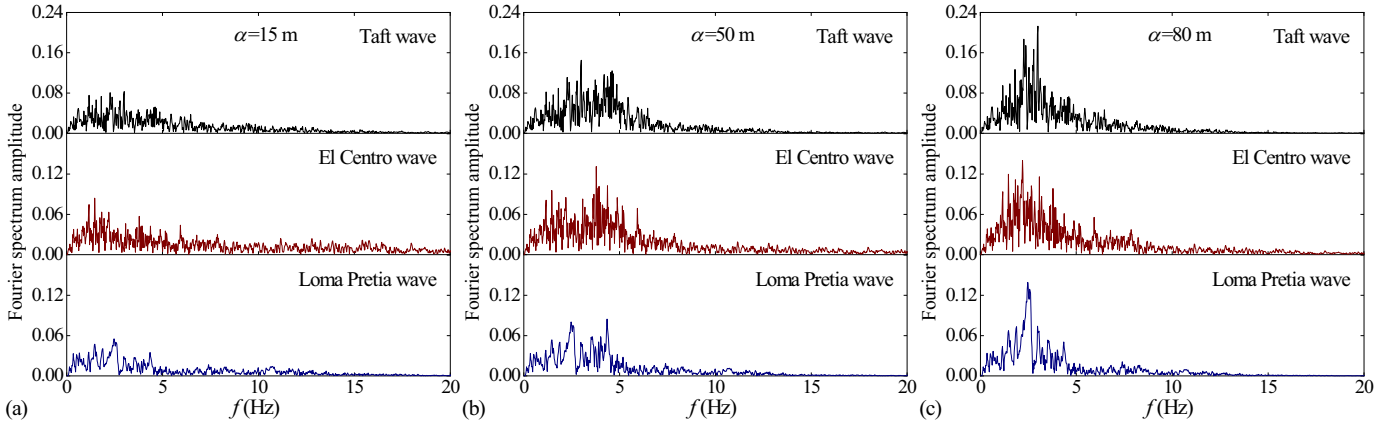

Fig. 16. Fourier amplitude spectra of rock slopes with different slope heights.

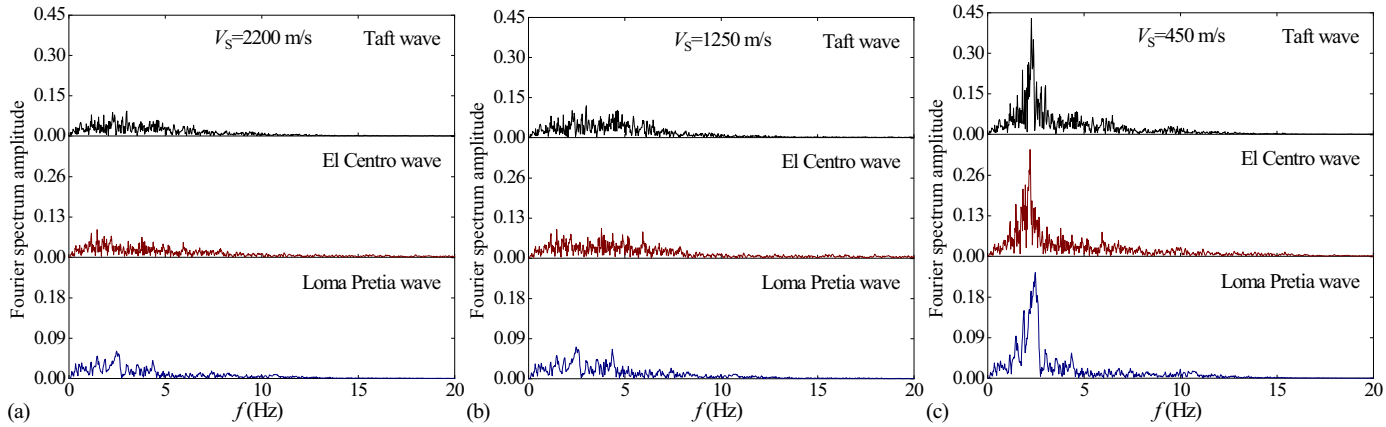

Fig. 17. Fourier amplitude spectra of rock slopes with different shear velocities.

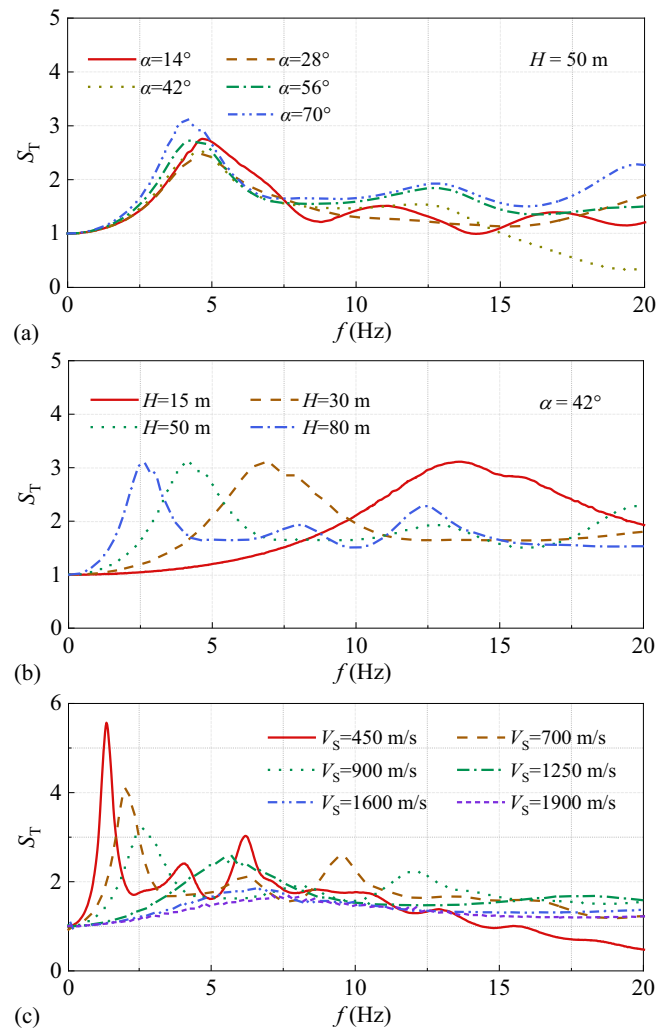

Fig. 18. Fourier spectral ratio curves at slope crest for different topographic and geological conditions. (a) Effect of geometric angle; (b) Effect of slope height; (c) Effect of shear velocity.

velocity V_S as an independent variable and amplification factor R_f for the slope crest as a dependent variable, the following expression is proposed as an empirical formula for the seismic response.

$$R_f = \frac{r_0}{1 + r_1 \cdot V_S} \tag{27}$$

The coefficients to be solved in Eq. (27) are r_0 and r_1. By using a concatenate fitting technique to process all data, the fitted curve for the influence of shear velocity on the amplification factor can be formulated as: $R_f = 3.73/(1 + 1.21 \cdot V_S)$.

4.3. Spectrum analysis of rock slope

4.3.1. Fourier spectrum

To analyze the spectral response characteristics in the site effect of rock slope, the Fourier spectra of slope crest with different geometric profiles and shear velocities are shown in Figs. 15–17, in which the remaining variables are taken as constant values when investigating the influence of one of them. Evidently, the geometry parameters and shear velocity significantly impact the spectral characteristics, and the spectrum response shares similar patterns for different input seismic waves. With the increase of slope angle, the Fourier spectrum has a weak increase in amplitude with no apparent difference in shape. As the slope height increases and the shear velocity decreases, the Fourier spectrum gradually increases in amplitude and shifts in shape from multiple peaks to a single peak feature. Moreover, the variation in slope height and shear velocity alters the predominant frequency of the slope site. Compared to the input wave features (see Fig. 6), the dominant frequency band corresponding to the spectral peak of various slope examples is also altered.

4.3.2. Spectral ratio curve

The spectral ratio curve is introduced to quantitatively evaluate the spectral amplification effect of rock slope, with the standard spectral ratio S_T is defined in Eq. (28) (Theodulidis and Bard, 1995). From the definition of fast Fourier transform and $a = \omega^2 u$, a spectral ratio curve can be equated to the displacement amplification in the frequency domain, independent of the type of input seismic waves.

$$S_T = \frac{S_{HS}}{S_{HB}} \tag{28}$$

where S_{HS} is the horizontal Fourier spectrum of the recorded motion on slope site, and S_{HB} is the horizontal Fourier spectrum of the recorded motion on bedrock outcropping.

The Fourier spectral ratio curves at slope crest for different topographic and geological conditions are given in Fig. 18. First, the pattern of S_T varying with frequency is similar for different slope angles (see Fig .18a, where $H = 50^\circ$ as an example), and the difference is mainly reflected in the peak ratio. Comparing the curves for all slope angles, a maximum S_T is 3.08 and a minimum S_T is 2.42, with a difference of 1.27

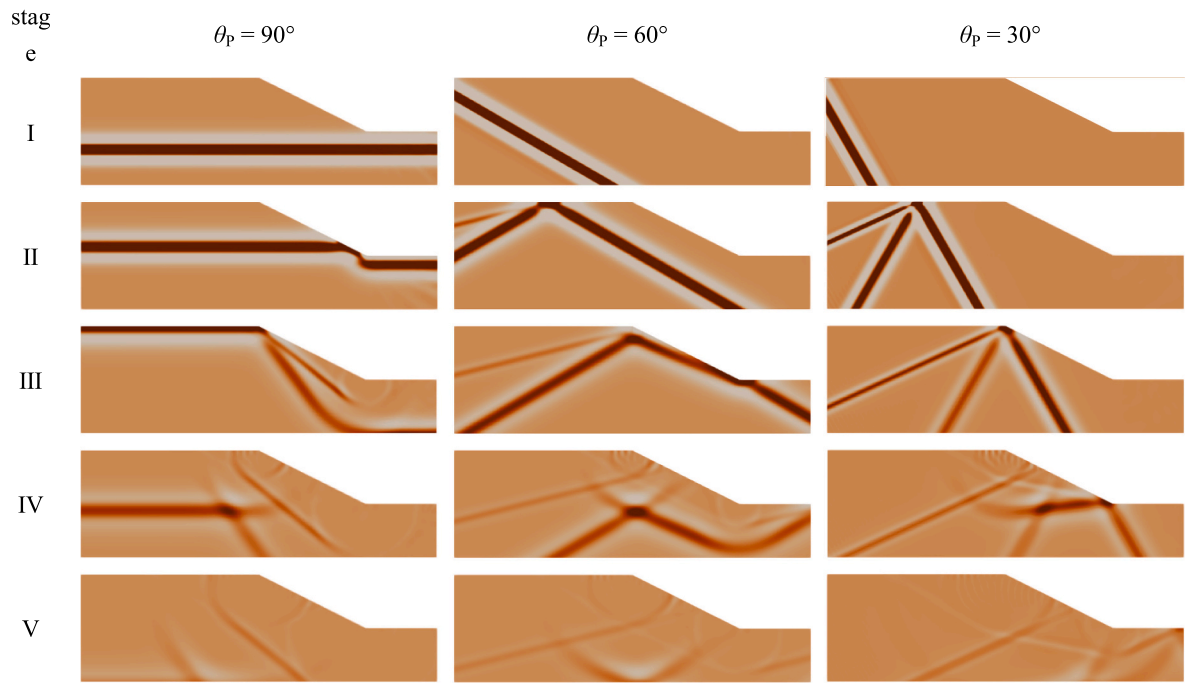

Fig. 19. Snapshots of the displacement wave field corresponding to a model slope with different incident wave angles.

times, can be noticed. Second, as the slope height increases, more abundant low-frequency components in the spectrogram, thus the difference is mainly reflected in corresponding peak frequency. Comparing the curves for all slope heights, it is revealed that the maximum of first peak frequency is 13.5 Hz, and the minimum case is 2.5 Hz, with a difference of 5.4 times. Finally, with the increase of the shear velocity (see Fig .18c), the peak of S_T gradually decreases, and the corresponding peak frequency moves from low-frequency to high-frequency. There may be a critical value, below which the curve decays very rapidly and the dominant frequencies are in the low-frequency band, and above which the decay rate slows down and the dominant components toward the middle and high frequencies. Analyzing the curves for all shear velocities reveals a difference of 3.62 times for S_T, and 3.46 times for first peak frequency.

5. Discussion on the applicability of the method

To test the broad applicability of the proposed method, this section discusses the variation of the wave field and spectral response of a single-layered slope for different incident frequencies and incident angles. Here, a model slope with a given slope height $H = 30$ m and slope angle $\alpha = 28°$ is used as an example, and the seismic source is considered as P waves with a Ricker wavelet shape. Since P waves mainly induce vertically oriented seismic responses, all results in this section are for the vertical components.

5.1. Sensitivity to incident angle

To visualize the propagation process of seismic waves in a slope site, we wrote a Python program to obtain the snapshots of displacement wave field corresponding to different incident angles for a single-layered slope at the same incident wave frequency of $f_0 = 10$ Hz. As illustrated in Fig. 19, the subplots from left to right are three angles of $\theta_P = 90°$, 60°, and 30° respectively, and from top to bottom are different propagation stages. A total of 10,131 receivers are deployed throughout the model slope, with a horizontal and vertical interval of 1 m.

One can find that the wave field of the slope is highly complex because it is determined by the wave reflection on both the horizontal slope surface (i.e., the flat region on both sides of the slope) and the inclined slope. To illustrate the interaction between the slope and the incident waves, we classify the whole process into roughly five stages. Taking $\theta_P = 60°$ as an example, the analysis is as follows (other cases can be similarly deduced). In stage I: the P-wave seismic source is effectively input from the bedrock outcrop into the model slope, where the free wave propagates correctly along the stated direction; in stage II, the incident P wave encounters a free surface, generating the reflected P wave and reflected SV wave; in stage III: these waves encounter an inclined slope, further generating new waveform conversions and exciting the scattered wave fields as they pass through the upper and lower corners of the slope; in stage IV: the free-field and scattered fields together form the total wave field, which becomes progressively more complex away from the slope surface; in stage V: the wavefront propagates out of the model slope and no waves return from the model bottom, as the proposed method itself precisely satisfies the Sommerfeld's radiation condition at infinity. Moreover, with the progression of each stage, the energy attenuation arising from material damping (here $\zeta = 0.05$) leads to a gradual lightening of the wavefront colour.

It is also shown that, the characteristics of wave propagation under oblique and vertical incidence are significantly different. The incident angle of seismic waves affects the arrival and amplitude of the wave field, resulting in a varying dynamic response of the slope. In fact, according to geometric relations and Snell's law, the ray paths of the incident and reflected waves are opposite when the residual angle of incident angle is greater (e.g., $\theta_P = 60°$ and 30°) or less (e.g., $\theta_P = 90°$) than the slope angle, which is consistent with the description by Fan et al. (2018b) using a numerical method for the wave field analysis. In summary, our method can reveal the effect of incident angle on the wave field and has good applicability for both oblique and vertical incidence.

In Fig. 20, we calculated the Fourier spectra for a single-layered slope at different incident angles, where three representative monitoring points, namely #1 (30 m, 15 m), #2 (0 m, 15 m) and #3 (−30 m, 15 m), are selected. The effect of slope angle on the spectrum in the model slope is noticeable and cannot be ignored. For monitoring point 1 (on the slope surface), the pattern is intuitive, showing a gradual decrease in peak amplitude as the incident angle decreases. For monitoring point 2 (inside the slope but close to slope surface), the spectrum distribution is

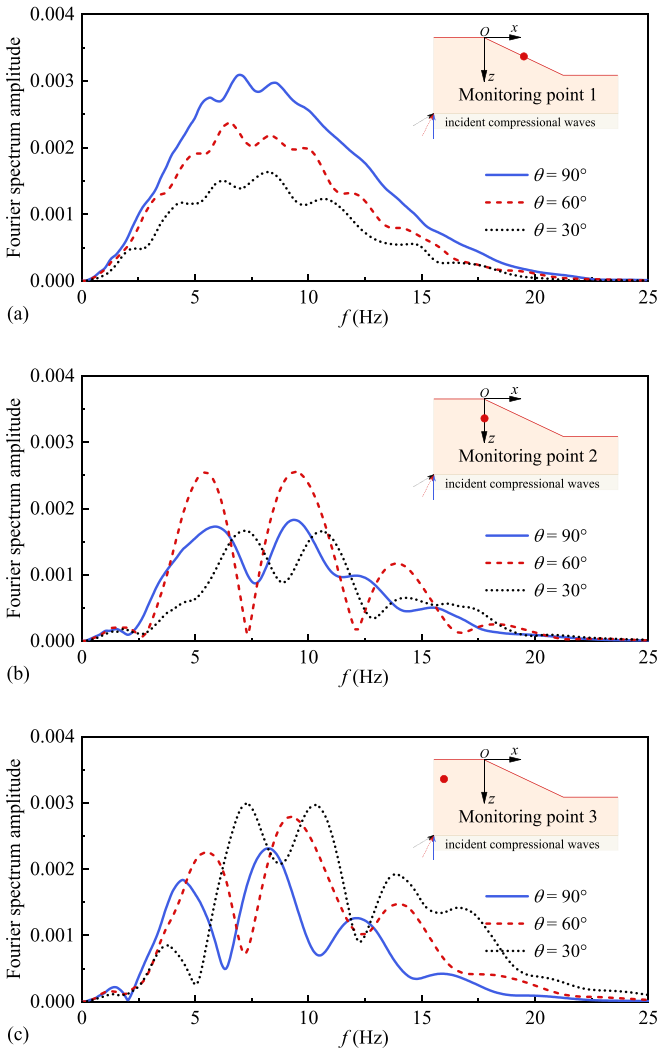

Fig. 20. Fourier spectra of a model slope for different incident angles, where three representative monitoring points, namely #1 (30 m, 15 m), #2 (0 m, 15 m) and #3 (−30 m, 15 m), are selected.

more complex, changing from a single to a double-peaked feature, with the maximum spectral response for the slope at $\theta_P = 60°$ among the three angles. For monitoring point 3 (inside the slope but away from slope surface), the spectral peaks and their distribution are more convoluted. This coincides with the variation in the wavefield (see Fig. 18), a state in which the spectral curve inside the slope is more oscillatory than that on the slope surface due to the combined effect of the incident, reflected and scattered waves.

5.2. Sensitivity to incident frequency

Fig. 21 shows the wave field snapshots corresponding to different incident wave frequencies at the same incident angle of $\theta_P = 45°$, where the subplots from left to right are three frequencies of $f_0 = 2$ Hz, 7 Hz and 12 Hz, respectively, and from top to bottom are three typical propagation stages. Evidently, the higher the incident frequency, the smaller the wavelength ($\lambda = V_S/f$) and the narrower the wavefront. Compared with the low-frequency case, the scattered wave field formed by the high-frequency incident wave is more pronounced, and decays faster. Fig. 22 further depicts the corresponding Fourier spectra curve, and three typical monitoring points are used for the analysis. For the given Ricker inputs with the same wavelet amplitude, the Fourier spectrum amplitude decreases with the increase of the center frequency, and its distribution gradually oscillates. Moreover, the frequency ranges of the slope response are significantly different, with the effective frequencies corresponding to the three incident waves being 0–5 Hz, 0–15 Hz, and 0–20 Hz, respectively.

The above analysis demonstrates that the proposed method is sensitive to incident wave frequency and can completely identify various frequency components. Notably, the semi-analytical solution has the merit of fast solving the influence of frequency on the slope, i.e., the calculation of the slope response only requires one time in the frequency-wavenumber domain. As a result, the time-history response in the space domain at different incident frequencies can be speedily obtained by performing the inverse Fourier transform again (see Eqs. (22) ~ (24)). Taking advantage of this, subsequent studies can focus on capturing the predominant frequencies of various actual slopes concerning natural seismic waves, and analyzing resonance-induced slope instability and damage to buildings on a slope, which is beneficial to the development of geotechnical earthquake engineering.

6. Application to an example

6.1. Analytical treatment of actual slope topography

On 12 May 2008, the Wenchuan M_S 8.0 earthquake occurred in southwestern China, with the epicenter located in the Longmenshan fault zone, which is densely populated by high mountains, steep slopes and deep valleys (Juang et al., 2015; Fan et al., 2018a). These local sites with extremely complex geological and topographical features, with large differences in elevation, undoubtedly had a significant impact on the seismic ground motion.

During the Wenchuan earthquake, multiple observation stations arranged on the Xishan slope (located in Xishan Park, Zigong City, Sichuan Province) obtained complete mainshock records, which filled the gaps of previous strong motion data from topographic arrays. These

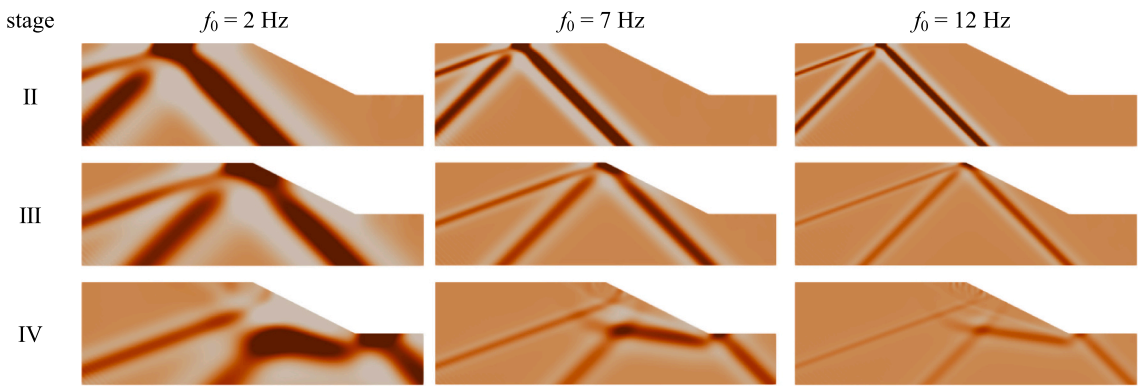

Fig. 21. Snapshots of the displacement wave field corresponding to a model slope with different incident wave frequencies.

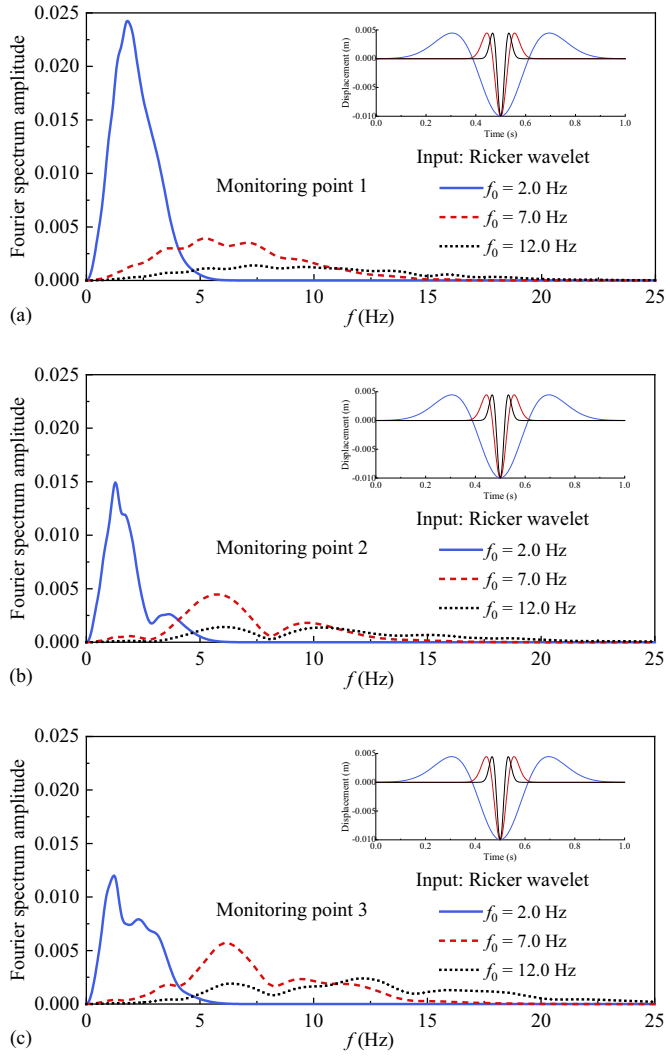

Fig. 22. Fourier spectra of a model slope for different incident frequencies, where three representative monitoring points, namely #1 (30 m, 15 m), #2 (0 m, 15 m) and #3 (−30 m, 15 m), are selected.

observatories were constructed and operated since 2007, mainly to monitor the non-uniformity in the spatial distribution of ground motion amplification by surface irregularities. All stations are installed on the rock slopes and outcropping rock, which provides valuable information for studying site effects and landslide stability. Among them, station 1 (*S*1) is situated at the outcropping rock of slope bottom and is generally assumed to be a reference point, while other stations are situated on the slope with different heights and are used for identifying seismic amplification. The geographical map and station arrangement of the region of interest are shown in Fig. 23.

In the analytical treatment of actual rock slope, the slope angle is estimated to be about 27° and the slope height is set to be 72 m based on the digital elevation of Xishan Park. The physical properties of the slope itself and the underlying strata can be described by the velocity structure obtained from the geological exploration information, as listed in Table 5. On the other hand, since the Xishan slope is approximately 226.4 km away from the epicenter of the Wenchuan earthquake, the seismic energy propagating to the region of interest is apparently generated by the teleseismic body waves as plane waves, and the angle of incidence may be close to vertical. As a result, an obliquely incident shear wave with a Ricker waveform at a large angle of 85° is assumed to be the seismic excitation. The analytical model established in this section is shown in Fig. 24.

6.2. Comparison with observation records

Fig. 25 presents a comparison of the horizontal components (NS direction) recorded at the observatory (Wang and Xie, 2010) with those obtained from the analytical model, where all the results are processed with the dimensionless spectral ratio (see Eq. (28)). In general, the spectral ratio curves calculated by the proposed semi-analytical approach are in reasonable agreement with the strong motion data, which broadly reflect the trends in ground motion caused by the variation of slope site conditions. For the low-frequency components less than 2 Hz, the amplification effect due to the presence of topography is obscure, and the traces of the two curves are quite consistent. When the frequency is greater than 2 Hz, a pronounced slope seismic effect can be noticed, and the amplitude distribution of the spectral ratios across the frequency band differs significantly between the stations. The comparison indicates that the presented semi-analytical solutions for station 2 and station 4 are similar to the observation records, while the calculated curves for station 3 and station 5 are to some extent an underestimate of the spectral variation at certain frequency features, but their maximum responses are still relatively close. This can be explained that the analytical model is treated as an ideal 2D rock slope, which cannot consider the influence of surface weathering layers and subsurface rock structural heterogeneity on seismic ground motion, hence some discrepancies between the theoretical values and the actual records.

Summarizing from this application example, it is evident that the semi-analytical approach presented in this paper can accurately tackle the seismic response of stratified rock slopes. In contrast to domain-based numerical schemes, this method avoids the division of the computational domain grid and the imposition of artificial absorbing boundaries. This allows for rapid acquisition of preliminary site effect characteristics, which can be used as a reference for analyzing geological hazards on slopes. We suggest a further understanding of the geological structure of the rock slope (e.g., discontinuous joints and weak structural planes), and the development of a more realistic 3D model with the aid of semi-analytical or numerical methods to obtain broadband ground motions.

7. Concluding remarks

A semi-analytical method is proposed to solve the seismic response of stratified rock slopes due to incident P and SV waves. Based on the verification of the accuracy and reliability of theoretical formulations, parametric studies of a slope site overlying bedrock half-space are first performed to explore the effects of the geometric profile and shear velocity on the slope surface dynamic responses. Some conclusions can be drawn as follows:

1. The seismic response of rock slopes has a significant elevation amplification effect. With the increase of relative elevation, the PGA amplification factor of slope surface shows a nonlinear increasing trend. The elevation effect of horizontal acceleration is mainly manifested in the middle and upper of the slope, while this pattern is more pronounced at smaller slope heights and geometric angles. Additionally, due to the interaction between the upper protruding topography and lower bedrock half-space, a decreasing effect exists in the dynamic response near the slope toe.
2. The acceleration responses of the rock slope crest are obviously affected by the geometry and shear velocity of the slope. With the increase of slope angle and slope height, the PGA generally increases, while with the increase of shear velocity, the PGA exhibits a decreasing trend. Therefore, depending on the calculation results under different input seismic waves, the empirical equations for slope response varying with geometric parameters and shear velocity are presented, which may serve as a reference for further quantitative analysis.

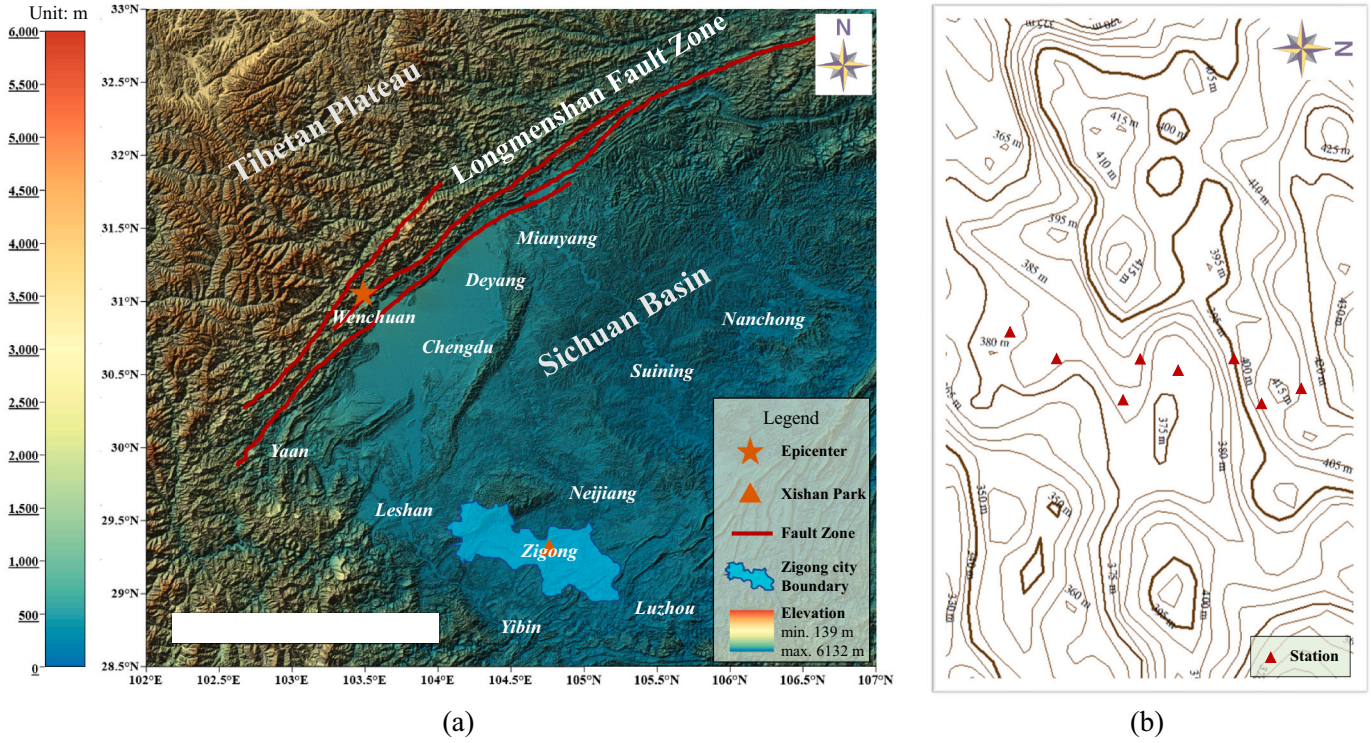

Fig. 23. Wenchuan earthquake and Xishan slope. (a) Regional tectonic map and topographic map of the Wenchuan earthquake; (b) Contour map of the topographic array at Xishan slope.

Table 5
Velocity structure of slope topography for the Xishan Park in Zigong, China.

Depth (m)	Density ρ (kg/m^3)	P-wave velocity V_P (m/s)	S-wave velocity V_S (m/s)	Poisson's ratio ν	Damping ζ
0–72	2000	1386	800	0.34	0.01
−8–0	2150	1154	617	0.37	0.01
−20 ~ −8	2360	1288	744	0.34	0.01
−60 ~ −20	2450	1956	1198	0.32	0.01
−∞	2650	2917	1839	0.25	0.005

Note: The symbol '−∞' represents the engineering bedrock.

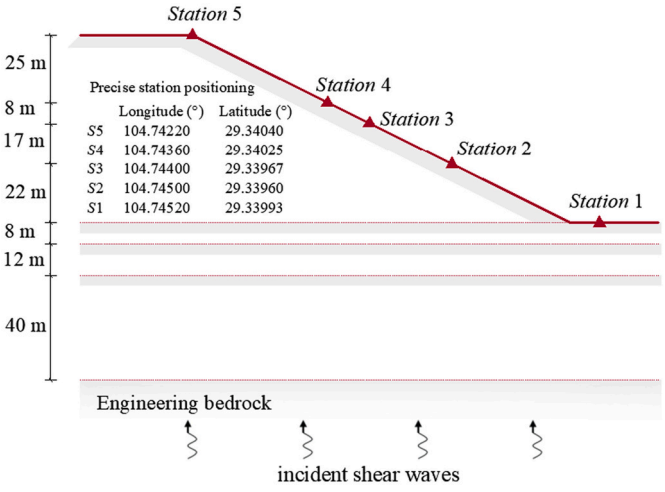

Fig. 24. A simplified analytical model of slope topography for the Xishan Park in Zigong, China.

3. The variation in spectra response of geometry and shear velocity of rock slopes is roughly analogous to their acceleration response. It can be observed that the slope angle has less influence on the spectral peak, shape and predominant frequency of Fourier spectra, while the slope height and shear velocity have a more pronounced impact on them. To quantitatively evaluate the amplification effect, the spectral ratio curve is introduced to obtain the amplification factor and peak frequency of ground motion of rock slopes with different parameters, which is helpful for further developing ground-motion prediction models.

Subsequently, to illustrate the broad applicability of the proposed method, sensitivity analyses are carried out on model slopes with varying incident wave frequencies and incident angles. Through visualization, it shows that the wave field of the slope is extremely complex, as it is determined by the wave reflection on both the horizontal slope surface and inclined slope. On the other hand, the free-field and scattered fields together form the total wave field, which becomes progressively more complex away from the slope surface. Also, the spectral curve inside the slope is more oscillatory than that on the slope surface due to the combined effect of the incident, reflected and scattered waves. All analyses indicate that the proposed method is sensitive to incident seismic waves and can completely identify various frequency components and oblique incidence.

Finally, a case study is conducted to evaluate the practicality of the proposed method, where the actual slope topography located in the Xishan Park in Zigong, China, is treated analytically as a simplified stratified rock slope. By comparison with observation records of the 2008 Wenchuan earthquake, it can be found that the spectral ratio curves calculated by the semi-analytical approach are in reasonable agreement with the strong motion data, which broadly reflect the trends in ground motion caused by the variation of slope site condition. The shortcoming, however, is that the presented methodology is derived from the theory of elastodynamics, which cannot consider the influence of surface weathering layers and subsurface rock structural

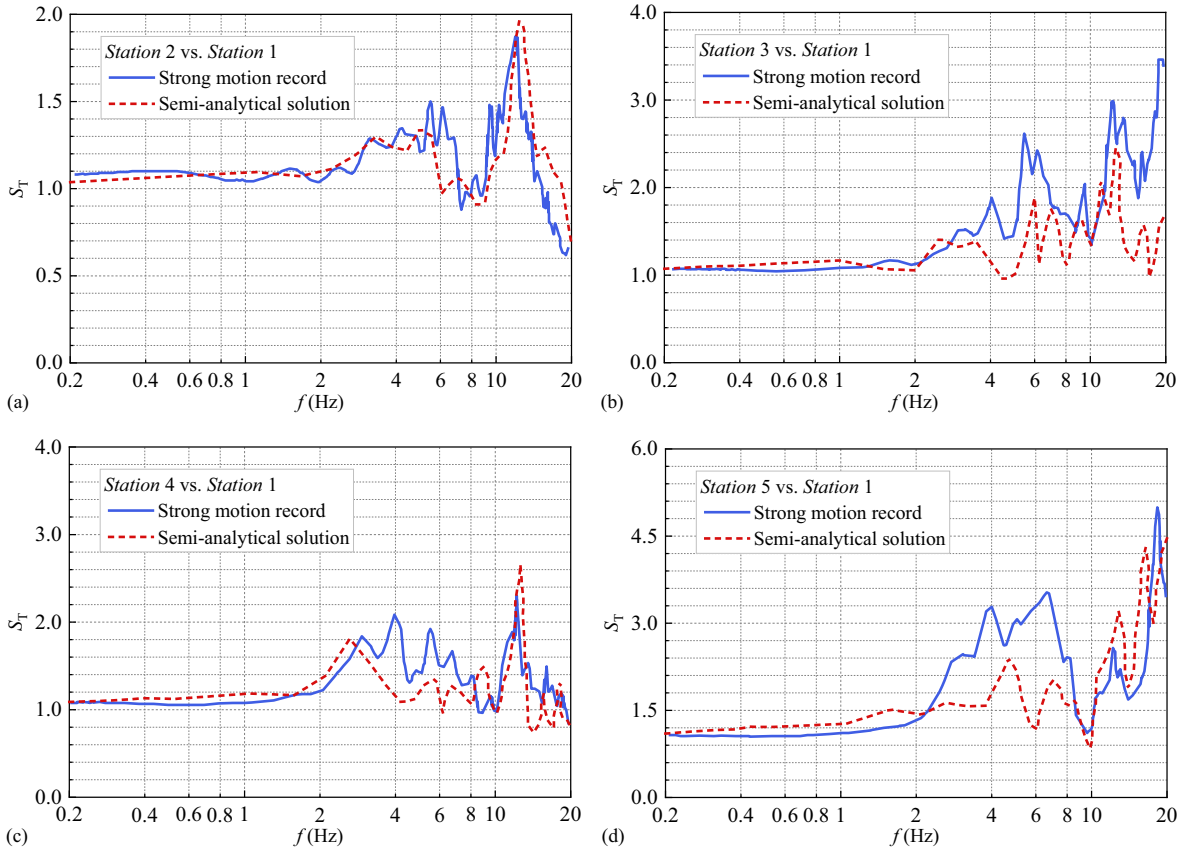

Fig. 25. Comparison of spectral amplification curves between numerical calculation and strong motion data.

heterogeneity on seismic ground motion, hence some discrepancies between the theoretical values and the actual records. We suggest a further understanding of topographic features, heterogeneous structures and weathered geology, and the development of a more realistic 3D model to obtain broadband ground motions of stratified rock slopes.

Declaration of Competing Interest

The authors declare that they have no known competing financial interests or personal relationships that could have appeared to influence the work reported in this paper.

Acknowledgments

The authors would like to acknowledge the Institute of Engineering Mechanics, China Earthquake Administration for making useful information available for this study. The authors would like to express their great appreciation to the respected Editor-in-Chief, the Editor, and the three anonymous reviewers for their valuable comments and precious time spent on this paper. The first author (M.T. Wu) is very grateful for the support provided by Prof. Jianwen Liang, Prof. Zhenning Ba, and Tianjin University. This study is sponsored by the following agencies: Research Fund of Institute of Engineering Mechanics, China Earthquake Administration under Grant no. 2019D25, Natural Science Foundation of Hunan Province under Grant no. 2020JJ6073, and the Postdoctoral Foundation of Hong Kong University.

References

Assefa, S., Graziani, A., Lembo-Fazio, A., 2017. A slope movement in a complex rock formation: Deformation measurements and DEM modeling. Eng. Geol. 219, 74–91.
Beskos, D.E., 1987. Boundary element methods in dynamic analysis. Appl. Mech. Rev. 40, 1–23.
Bhasin, R., Kaynia, A.M., 2004. Static and dynamic simulation of a 700-m high rock slope in western Norway. Eng. Geol. 71 (3–4), 213–226.
Bolla, A., Paronuzzi, P., 2020. Geomechanical field survey to identify an unstable rock slope: the Passo della Morte case history (NE Italy). Rock Mech. Rock. Eng. 53 (4), 1521–1544.
Bouchon, M., Sánchez-Sesma, F.J., 2007. Boundary integral equations and boundary elements methods in elastodynamics. Adv. Geophys. 48, 157–189.
Bouckovalas, G.D., Papadimitriou, A.G., 2005. Numerical evaluation of slope topography effects on seismic ground motion. Soil Dyn. Earthq. Eng. 25 (7–10), 547–558.
Chandra, R., Dagum, L., Kohr, D., Menon, R., Maydan, D., McDonald, J., 2001. Parallel programming in OpenMP. Morgan kaufmann, San Francisco.
Chen, C.C., Li, H.H., Chiu, Y.C., Tsai, Y.K., 2020. Dynamic response of a physical anti-dip rock slope model revealed by shaking table tests. Eng. Geol. 277, 105772.
Chigira, M., Wu, X., Inokuchi, T., Wang, G., 2010. Landslides induced by the 2008 Wenchuan earthquake, Sichuan, China. Geomorphology 118 (3–4), 225–238.
Davis, L.L., West, L.R., 1973. Observed effects of topography on ground motion. Bull. Seismol. Soc. Am. 63 (1), 283–298.
Degrande, G., 2002. Wave propagation in the soil: Theoretical background and application to traffic induced vibrations. In: Proceedings of the 5th European Conference on Structural dynamics.
Del Gaudio, V., Wasowski, J., 2007. Directivity of slope dynamic response to seismic shaking. Geophys. Res. Lett. 34 (12), L12301.
Eshraghi, H., Dravinski, M., 1989. Scattering of plane harmonic SH, SV, P and Rayleigh waves by non-axisymmetric three-dimensional canyons: a wave function expansion approach. Earthq. Eng. Struct. Dyn. 18 (7), 983–998.
Fan, X., Juang, C.H., Wasowski, J., Huang, R., Xu, Q., Scaringi, G., Havenith, H. B., 2018a. What we have learned from the 2008 Wenchuan Earthquake and its aftermath: a decade of research and challenges. Eng. Geol. 241, 25–32.
Fan, G., Zhang, L.M., Li, X.Y., Fan, R.L., Zhang, J.J., 2018b. Dynamic response of rock slopes to oblique incident SV waves. Eng. Geol. 247, 94–103.
Haskell, N.A., 1953. The dispersion of surface waves on multilayered media. Bull. Seismol. Soc. Am. 43 (1), 17–34.
Huang, R., Lin, F., Yan, M., 2010. Deformation mechanism and stability evaluation for the left abutment slope of Jinping I hydropower station. Bull. Eng. Geol. Environ. 69 (3), 365–372.
Huang, H., Gong, W., Khoshnevisan, S., Juang, C.H., Zhang, D., Wang, L., 2015. Simplified procedure for finite element analysis of the longitudinal performance of shield tunnels considering spatial soil variability in longitudinal direction. Comput. Geotech. 64, 132–145.
Juang, C.H., Zhang, J., Gong, W., 2015. Reliability-based assessment of stability of slopes. In: IOP Conference Series: Earth and Environmental Science, vol. 26. IOP Publishing, p. 012006. No. 1. August.

Kausel, E., Roësset, J.M., 1981. Stiffness matrices for layered soils. Bull. Seismol. Soc. Am. 71 (6), 1743–1761.
Li, D.Q., Jiang, S.H., Cao, Z.J., Zhou, C.B., Li, X.Y., Zhang, L.M., 2015. Efficient 3-D reliability analysis of the 530 m high abutment slope at Jinping I Hydropower Station during construction. Eng. Geol. 195, 269–281.
Lin, M.L., Wang, K.L., 2006. Seismic slope behavior in a large-scale shaking table model test. Eng. Geol. 86 (2–3), 118–133.
Liu, H., Xu, Q., Li, Y., Fan, X., 2013. Response of high-strength rock slope to seismic waves in a shaking table test. Bull. Seismol. Soc. Am. 103 (6), 3012–3025.
Liu, H.X., Xu, Q., Li, Y.R., 2014. Effect of lithology and structure on seismic response of steep slope in a shaking table test. J. Mt. Sci. 11 (2), 371–383.
Liu, Q., Wu, Z., Lee, V.W., 2019. Scattering and reflection of SH waves around a slope on an elastic wedged space. Earthq. Eng. Eng. Vib. 18 (2), 255–266.
Lu, Y., Tan, Y., Li, X., 2018. Stability analyses on slopes of clay-rock mixtures using discrete element method. Eng. Geol. 244, 116–124.
Song, D., Chen, Z., Ke, Y., Nie, W., 2020. Seismic response analysis of a bedding rock slope based on the time-frequency joint analysis method: a case study from the middle reach of the Jinsha River, China. Eng. Geol. 274, 105731.
Tang, C., Zhu, J., Qi, X., Ding, J., 2011. Landslides induced by the Wenchuan earthquake and the subsequent strong rainfall event: a case study in the Beichuan area of China. Eng. Geol. 122 (1–2), 22–33.
Theodulidis, N.P., Bard, P.Y., 1995. Horizontal to vertical spectral ratio and geological conditions: an analysis of strong motion data from Greece and Taiwan (SMART-1). Soil Dyn. Earthq. Eng. 14 (3), 177–197.
Thomson, W.T., 1950. Transmission of elastic waves through a stratified solid medium. J. Appl. Phys. 21 (2), 89–93.
Wang, H.Y., Xie, L.L., 2010. Effects of topography on ground motion in the Xishan park, Zigong city. Chin. J. Geophys. 53 (7), 1631–1638.
Wolf, J.P., 1985. Dynamic Soil-Structure Interaction. Prentice-Hall, Englewood Cliffs.
Wolf, J.P., Obernhuber, P., 1982. Free-field response from inclined SV-and P-waves and Rayleigh-waves. Earthq. Eng. Struct. Dyn. 10 (6), 847–869.
Xiao, J., Gong, W., Martin II, J.R., Shen, M., Luo, Z., 2016. Probabilistic seismic stability analysis of slope at a given site in a specified exposure time. Eng. Geol. 212, 53–62.
Xu, Q., Fan, X.M., Huang, R.Q., Van Westen, C., 2009. Landslide dams triggered by the Wenchuan Earthquake, Sichuan Province, south west China. Bull. Eng. Geol. Environ. 68 (3), 373–386.
Yang, J., 2002. Saturation effects of soils on ground motion at free surface due to incident SV waves. J. Eng. Mech-ASCE 128 (12), 1295–1303.
Yang, J., Yan, X.R., 2009a. Site response to multi-directional earthquake loading: a practical procedure. Soil Dyn. Earthq. Eng. 29 (4), 710–721.
Yang, J., Yan, X.R., 2009b. Factors affecting site response to multi-directional earthquake loading. Eng. Geol. 107 (3–4), 77–87.
Yang, G., Qi, S., Wu, F., Zhan, Z., 2018. Seismic amplification of the anti-dip rock slope and deformation characteristics: a large-scale shaking table test. Soil Dyn. Earthq. Eng. 115, 907–916.
Yin, Y., Wang, F., Sun, P., 2009. Landslide hazards triggered by the 2008 Wenchuan earthquake, Sichuan, China. Landslides 6 (2), 139–152.
Zhang, C., Liu, Q., Deng, P., 2017. Surface motion of a half-space with a semicylindrical canyon under P, SV, and Rayleigh waves. Bull. Seismol. Soc. Am. 107 (2), 809–820.
Zhang, Y., Zhang, J., Chen, G., Zheng, L., Li, Y., 2015. Effects of vertical seismic force on initiation of the Daguangbao landslide induced by the 2008 Wenchuan earthquake. Soil Dyn. Earthq. Eng. 73, 91–102.
Zhao, L., Huang, Y., Hu, H., 2020. Stochastic seismic response of a slope based on large-scale shaking-table tests. Eng. Geol. 277, 105782.
Zhi, W., Huang, R., Liu, C., Su, J., 2015. The internal relations of the generation between the 2013Lushan (Ms 7.0) and 2008 Wenchuan (Ms 8.0) Earthquakes, China. In: International Symposium on Mega Earthquake Induced Geo-disasters & Longterm Effects.
Zhu, C., He, M., Karakus, M., Cui, X., Tao, Z., 2020. Investigating toppling failure mechanism of anti-dip layered slope due to excavation by physical modelling. Rock Mech. Rock. Eng. 53 (11), 5029–5050.